New Journal of Physics
The open access journal at the forefront of physics
Deutsche Physikalische Gesellschaft DPG IOP Institute of Physics

PAPER • OPEN ACCESS

Coherence protection and decay mechanism in qubit ensembles under concatenated continuous driving

To cite this article: Guoqing Wang *et al* 2020 *New J. Phys.* **22** 123045

New Journal of Physics
The open access journal at the forefront of physics

Deutsche Physikalische Gesellschaft DPG
IOP Institute of Physics

Published in partnership with: Deutsche Physikalische Gesellschaft and the Institute of Physics

CrossMark

OPEN ACCESS

RECEIVED
25 August 2020

REVISED
8 December 2020

ACCEPTED FOR PUBLICATION
11 December 2020

PUBLISHED
30 December 2020

PAPER

Coherence protection and decay mechanism in qubit ensembles under concatenated continuous driving

Guoqing Wang(王国庆)[1], Yi-Xiang Liu(刘仪襄)[1] and Paola Cappellaro[1,2,*]

[1] Research Laboratory of Electronics and Department of Nuclear Science and Engineering, Massachusetts Institute of Technology, Cambridge, MA 02139, United States of America

[2] Department of Physics, Massachusetts Institute of Technology, Cambridge, MA 02139, United States of America

[*] Author to whom any correspondence should be addressed.

E-mail: pcappell@mit.edu

Keywords: coherence protection, concatenated continuous driving, generalized Bloch equation, noise spectrum, nitrogen-vacancy ensembles, quantum control, Mollow triplet

Abstract

Dense ensembles of spin qubits are valuable for quantum applications, even though their coherence protection remains challenging. Continuous dynamical decoupling can protect ensemble qubits from noise while allowing gate operations, but it is hindered by the additional noise introduced by the driving. Concatenated continuous driving (CCD) techniques can, in principle, mitigate this problem. Here we provide deeper insights into the dynamics under CCD, based on Floquet theory, that lead to optimized state protection by adjusting driving parameters in the CCD scheme to induce mode evolution control. We experimentally demonstrate the improved control by simultaneously addressing a dense nitrogen-vacancy (NV) ensemble with 10^{10} spins. We achieve an experimental 15-fold improvement in coherence time for an arbitrary, unknown state, and a 500-fold improvement for an arbitrary, known state, corresponding to driving the sidebands and the center band of the resulting Mollow triplet, respectively. We can achieve such coherence time gains by optimizing the driving parameters to take into account the noise affecting our system. By extending the generalized Bloch equation approach to the CCD scenario, we identify the noise sources that dominate the decay mechanisms in NV ensembles, confirm our model by experimental results, and identify the driving strengths yielding optimal coherence. Our results can be directly used to optimize qubit coherence protection under continuous driving and bath driving, and enable applications in robust pulse design and quantum sensing.

1. Introduction

Scaling up the size of quantum systems is desirable in many quantum technologies, ranging from quantum simulators to quantum sensors. However, manipulating a large quantum system while simultaneously protecting the coherence remains challenging, even when the quantum application only requires collective control, such as some special ensemble-based quantum sensors or simulators. In particular, frequency and driving inhomogeneities typically increase when the system size increases. Various techniques such as pulsed and continuous dynamical decoupling [1–17], as well as spin-locking [18] have been used to protect the coherence of quantum systems.

Beyond achieving robust quantum memories, manipulating the quantum device while maintaining its coherence remains a non-trivial task [19], but could be helped by using continuous decoupling schemes. Unfortunately, these often introduce additional sources of noise linked to the added driving fields. A technique termed concatenated continuous driving (CCD), which consists of adding multiple resonant modulated fields, can combat external noise and fluctuations in the control fields [20–30]. A modulation field on resonance with the main driving term can suppress decoherence, provided that its amplitude is much larger than the fluctuations of the main driving.

Here, we use the CCD scheme to protect the coherence of an ensemble of qubits and to achieve their collective manipulation in the presence of frequency and driving field inhomogeneities. Experimentally, we achieve a 15-fold improvement in the coherence time for an arbitrary, unknown state (corresponding to the transverse coherence time) and we also show how to tune the CCD control to protect an arbitrary, known state with a 500-fold improvement in its coherence. These results are achieved through a more comprehensive understanding of the modulated dynamics, which can be described by Floquet theory as giving rise to a Mollow triplet [31]. A strong modulation has been demonstrated to have a broad feature in the synchronization by evaluating the power and detuning dependence of the evolution amplitude.

The long coherence times we achieve are also predicated on selecting the optimal control parameters given the characteristics of the noise. We thus carefully characterize the experimental noise sources by evaluating the power and detuning dependences of the Rabi signal coherence, and analyze the noise effects under the CCD scheme by extending the theoretical framework of the generalized Bloch equation (GBE) to this scenario. This analysis, confirmed by experimental results, allows not only to optimize the coherence time by adjusting the drive parameters, but it could be also used to reconstruct the PSD of various noise sources. Finally, we briefly discuss the potential applications in the protection of nuclear spin coherence, perfect pulse design and AC magnetic field sensing.

2. Coherence protection with the CCD scheme

2.1. Setup

Nitrogen-vacancy (NV) centers in diamond have emerged as a promising platform for quantum information processing [32], thanks in part to good control techniques that have pushed their coherence times nearly up to the relaxation limit [20, 24, 28, 30, 33–37]. Our device is based on an ensemble of NV centers in diamond as previously reported in reference [38] (see figure 1(a) for a schematic of the setup). The NV centers are contained within a 13 μm-thick surface layer on the diamond chip, consisting of isotopically purified diamond with 99.999% ^{12}C and a 20 ppm ^{14}N concentration. A pair of permanent magnets apply a static magnetic field along the NV axis, $B_0 \approx 230$ G, which lifts the degeneracy of the $|m_S = \pm 1\rangle$ states. The energy gap between the $|m_S = 0\rangle$ and $|m_S = -1\rangle$ states that we address in experiments is 2.207 GHz when the ^{14}N nuclear spin is in state $|m_I = 1\rangle$. Laser illumination not only initializes the NV electronic spin in the $|m_S = 0\rangle$ state, but also polarizes the ^{14}N nuclear spin states to 73% in $|m_I = 1\rangle$. Microwave is delivered through a 0.7 mm loop structure on a PCB board. Three photodiodes are attached to the surface of the diamond, and glued on the same PCB to measure the fluorescence. By focusing a 0.2 W green laser beam to a 30 μm spot, we simultaneously address $\sim 10^{10}$ spins. An arbitrary waveform generator mixes a $\sim$100 MHz frequency with a carrier microwave frequency generated by a signal generator to implement the coherent control. By applying a resonant microwave, we selectively address NV electronic spin $|m_S = 0\rangle$ and $|m_S = -1\rangle$ as the logical $|0\rangle$ and $|1\rangle$ states of an effective qubit.

2.2. Coherence protection

Due to field and driving inhomogeneities across the sample, as well as the presence of a spin bath, the coherence time under normal Rabi driving is about 1 μs (see figure 1(c) upper panel). To increase the coherence time we use a CCD scheme, whose basic principles are shown in figure 1(b). Consider a two-level system with a static splitting ω_0 along z, coupled to an amplitude-modulated microwave along the x axis, $\omega_{\mu w} = \Omega\cos(\omega t + \phi_0) + 2\epsilon_m \sin(\omega t + \phi_0)\sin(\omega_m t - \theta_m)$. The system Hamiltonian is then $H = \frac{\omega_0}{2}\sigma_z + \omega_{\mu w}\sigma_x$. In the (first) rotating frame defined by $H_0 = \frac{\omega}{2}\sigma_z$, the interaction picture Hamiltonian, $H_I = e^{\int_0^t iH_0 dt'} H\, e^{-\int_0^t iH_0 dt'} - H_0$, includes two parts $H_I = H_{I,C} + H_{I,CR}$, with the co-rotating part

$$H_{I,C} = -\frac{\delta}{2}\sigma_z + \frac{\Omega}{2}\left[\cos(\phi_0)\sigma_x + \sin(\phi_0)\sigma_y\right] - \epsilon_m \sin(\omega_m t - \theta_m)\left[\cos(\phi_0)\sigma_y - \sin(\phi_0)\sigma_x\right] \tag{1}$$

and the counter-rotating part

$$\begin{aligned} H_{I,CR} = \frac{\Omega}{2}&\left[\cos(2\omega t + \phi_0)\sigma_x - \sin(2\omega t + \phi_0)\sigma_y\right] \\ &+ \epsilon_m \sin(\omega_m t - \theta_m)\left[\cos(2\omega t + \phi_0)\sigma_y + \sin(2\omega t + \phi_0)\sigma_x\right] \end{aligned} \tag{2}$$

where in this work we assume a small detuning $\delta = \omega - \omega_0 \ll \Omega$. When the driving field amplitudes are much smaller than the energy gap, i.e. $\Omega, \epsilon_m \ll \omega$, the rotating wave approximation (RWA) is valid and counter-rotating term $H_{I,CR}$ in equation (2), oscillating at a high frequency 2ω, can be neglected. Thus, the Hamiltonian H_I under the RWA condition reduces to $H_{I,C}$ in equation (1). We can engineer a similar Hamiltonian through a phase-modulated waveform $\omega_\phi = \Omega\cos\left[\omega t + \phi_0 - \frac{2\epsilon_m}{\Omega}\sin(\omega_m t - \theta_m)\right]$. The

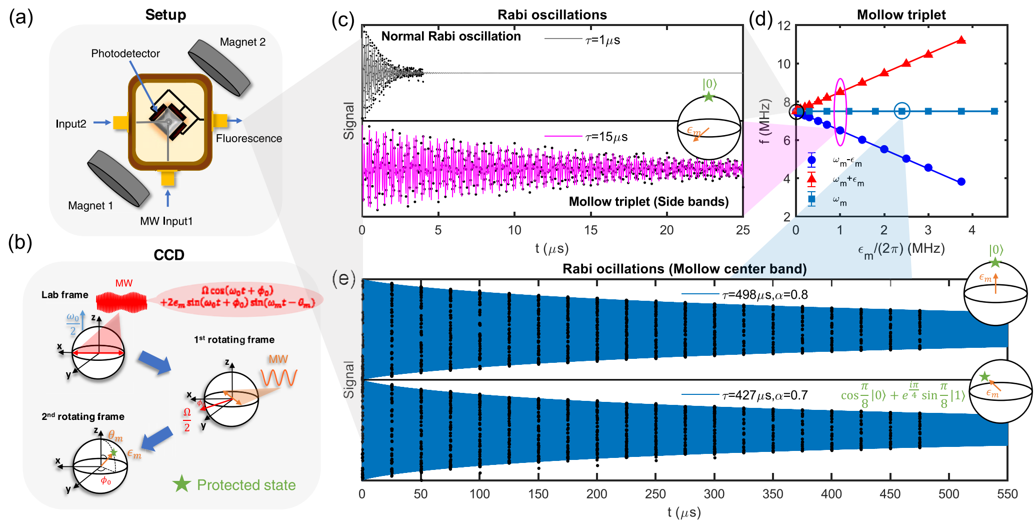

Figure 1. CCD for coherence protection. (a) Schematic of the experimental setup. (b) Principle of the amplitude-modulated CCD scheme. Upon applying a modulated waveform, we can enter into two rotating frames where direction and strength of the driving field can be set by the modulation parameters $\epsilon_{\mathrm{m}}, \phi_0, \theta_{\mathrm{m}}$. (c) Coherence protection of the Mollow triplet sidebands with the phase-modulated CCD scheme. Parameters $\Omega = \omega_{\mathrm{m}} = (2\pi)7.5$ MHz, $\theta_{\mathrm{m}} = \frac{\pi}{2}$ are chosen such that the effective driving field in the second rotating frame is perpendicular to the initial state $|0\rangle$. Upper panel is a normal Rabi oscillation with $\epsilon_{\mathrm{m}} = 0$. Lower panel is with $\epsilon_{\mathrm{m}} = (2\pi)1$ MHz. Coherence times τ_i are fitted with $c_0 + \sum_i c_i\,\mathrm{e}^{-\frac{t}{\tau_i}}\cos(\omega_i t + \phi_i)$. (d) Mollow triplet in the CCD scheme. Parameters $\Omega = \omega_{\mathrm{m}} = (2\pi)7.5$ MHz, and initial state is prepared to $|0\rangle$. Sidebands are measured with $\theta_{\mathrm{m}} = \frac{\pi}{2}$ and center band is measured with $\theta_{\mathrm{m}} = 0$. Frequency values are fitted from the Rabi oscillations with the same function as in (c). Solid lines are the theoretical predictions of the frequency values $\omega_{\mathrm{m}}, \omega_{\mathrm{m}} \pm \epsilon_{\mathrm{m}}$. (e) Coherence protection of the center band. Modulation strength $\epsilon_{\mathrm{m}} = (2\pi)2.4$ MHz. The driving field in the second rotating frame is adjusted to the same direction as the initial state such that the evolution will only involve the center band. In upper panel, the initial state is $|0\rangle$ and the driving parameters are $\phi_0 = 0, \theta_{\mathrm{m}} = 0$. In lower panel, the initial state is $\cos\left(\frac{\pi}{8}\right)|0\rangle + \mathrm{e}^{\mathrm{i}\frac{\pi}{4}}\sin(\frac{\pi}{8})|1\rangle$ and the driving parameters are $\phi_0 = -\frac{\pi}{4}, \theta_{\mathrm{m}} = \frac{\pi}{4}$. Coherence time τ and index α are fitted with $c_0 + c_1\,\mathrm{e}^{-(\frac{t}{\tau})^{\alpha}}\cos(\omega_1 t + \phi_1)$.

corresponding Hamiltonian, $H = \frac{\omega_0}{2}\sigma_z + \omega_\phi\sigma_x$, can be written in the first rotating frame defined by $H_0(t) = \frac{\omega}{2}\sigma_z - \frac{\epsilon_{\mathrm{m}}\omega_{\mathrm{m}}}{\Omega}\cos(\omega_{\mathrm{m}}t - \theta_{\mathrm{m}})\sigma_z$, as

$$H_{\mathrm{I}} = -\frac{\delta}{2}\sigma_z + \frac{\Omega}{2}\left[\cos(\phi_0)\sigma_x + \sin(\phi_0)\sigma_y\right] + \epsilon_{\mathrm{m}}\frac{\omega_{\mathrm{m}}}{\Omega}\cos(\omega_{\mathrm{m}}t - \theta_{\mathrm{m}})\sigma_z, \tag{3}$$

assuming again that the RWA is valid.

For both cases, the Hamiltonian in the interaction picture H_{I} includes a static field and a single-tone oscillating field, which is similar to the Hamiltonian in a standard continuous driving protocol. In the following we will thus describe only the amplitude modulation case.

Consider first for simplicity $\phi_0 = 0$. The (first) rotating frame Hamiltonian H_{I} reduces to $H_{\mathrm{I}} = \frac{\Omega_R}{2}\sigma'_x - \epsilon_{\mathrm{m}}\sin(\omega_{\mathrm{m}}t - \theta_{\mathrm{m}})\sigma'_y$, where $\Omega_{\mathrm{R}} = \sqrt{\Omega^2 + \delta^2}$ and $\sigma'_x = \frac{\Omega}{\Omega_{\mathrm{R}}}\sigma_x - \frac{\delta}{\Omega_{\mathrm{R}}}\sigma_z, \sigma'_y = \sigma_y, \sigma'_z = \frac{\Omega}{\Omega_{\mathrm{R}}}\sigma_z + \frac{\delta}{\Omega_{\mathrm{R}}}\sigma_x$. We can apply a second rotating-frame transformation defined by the Hamiltonian $H_0^{(2)} = \frac{\omega_{\mathrm{m}}}{2}\sigma'_x$. Assuming $\theta_{\mathrm{m}} = \frac{\pi}{2}$, the Hamiltonian in the second rotating frame, $H_{\mathrm{I}}^{(2)} = \mathrm{e}^{\mathrm{i}H_0^{(2)}t}H_{\mathrm{I}}\,\mathrm{e}^{-\mathrm{i}H_0^{(2)}t} - H_0^{(2)}$, is

$$H_{\mathrm{I}}^{(2)} = \frac{\Omega_{\mathrm{R}} - \omega_{\mathrm{m}}}{2}\sigma'_x + \frac{\epsilon_{\mathrm{m}}}{2}\sigma'_y + \frac{\epsilon_{\mathrm{m}}}{2}\left[\cos(2\omega_{\mathrm{m}}t)\sigma'_y - \sin(2\omega_{\mathrm{m}}t)\sigma'_z\right]. \tag{4}$$

For small detuning, $\Omega_{\mathrm{R}} - \omega_{\mathrm{m}} \ll \epsilon_{\mathrm{m}}$, and when the second RWA condition $\epsilon_{\mathrm{m}} \ll \omega_{\mathrm{m}}$ is satisfied, the term oscillating with frequency $2\omega_{\mathrm{m}}$ can be neglected and this gives rise to Rabi oscillations. In general, the oscillations display contributions from a center band ω_{m} and two sidebands $\omega_{\mathrm{m}} \pm \sqrt{\epsilon_{\mathrm{m}}^2 + (\omega_{\mathrm{m}} - \Omega_{\mathrm{R}})^2}$, forming the Mollow triplet (figure 1(d)) [31]. We can tune the relative intensity of the three bands by adjusting the phases $\phi_0, \theta_{\mathrm{m}}$ of the driving (*mode control*) [31]. Assuming now for simplicity that resonance conditions are satisfied ($\delta = 0, \omega_{\mathrm{m}} = \Omega_{\mathrm{R}} = \Omega, \sigma'_x = \sigma_x, \sigma'_y = \sigma_y, \sigma'_z = \sigma_z$), in the second rotating frame the RWA Hamiltonian reduces to a static driving field $H_{\mathrm{I}}^{(2)} = \frac{\epsilon_{\mathrm{m}}}{2}[\sin(\theta_{\mathrm{m}})(\cos(\phi_0)\sigma_y - \sin(\phi_0)\sigma_x) + \cos(\theta_{\mathrm{m}})\sigma_z]$, characterized by the polar and azimuthal angles $(\theta_{\mathrm{m}}, \phi_0)$. When the initial state is aligned with this static field, i.e. $|\psi(0)\rangle = \cos\left(\frac{\theta_{\mathrm{m}}}{2}\right)|0\rangle + \mathrm{e}^{\mathrm{i}\left(\phi_0 + \frac{\pi}{2}\right)}\sin\left(\frac{\theta_{\mathrm{m}}}{2}\right)|1\rangle$, it will not evolve in the second rotating frame: we call this the 'spin-locking' condition [18, 31]. Then, we only observe the evolution due to the rotating frame transformation, with oscillations at the frequency ω_{m}, the center band of the Mollow triplet. When the initial state is instead perpendicular to the static field, the evolution in the first rotating frame will be a

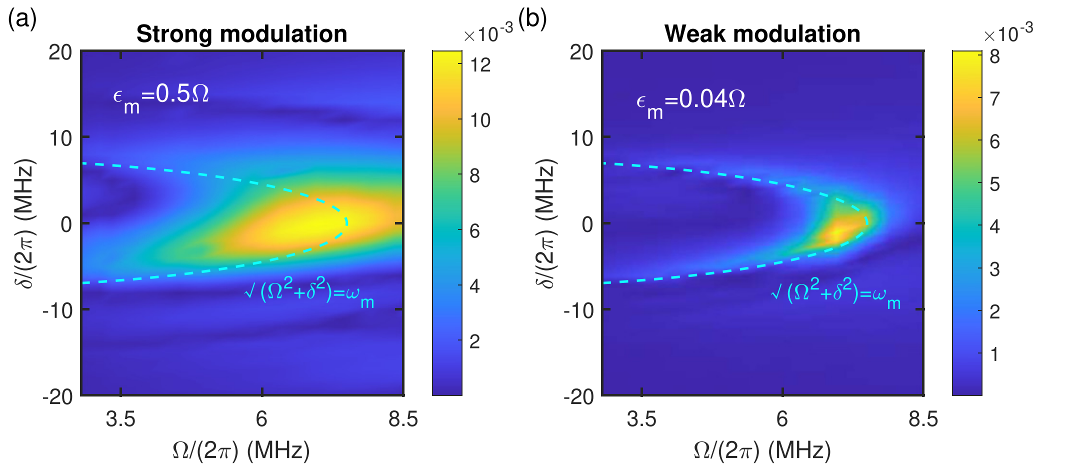

Figure 2. Synchronization of a single mode evolution. (a) Power and detuning dependence of the center band oscillation amplitude. Initial state is prepared to $|0\rangle$ and modulation frequency is $\omega_\mathrm{m} = (2\pi)7.5$ MHz. An amplitude-modulated CCD waveform is applied with a strong modulation condition $\epsilon_\mathrm{m} = \frac{1}{2}\Omega$ kept unchanged. $\theta_\mathrm{m} = 0$ such that the evolution is synchronized to the center band when $\Omega = \omega_\mathrm{m}, \delta = 0$. Rabi oscillations are measured from 50 μs to 50.5 μs to ensure that only the center band is alive. The intensity represents the value of contrast c_1 fitted from Rabi oscillations with $c_0 + \frac{1}{2}c_1\,\cos(\omega_1 t + \phi_1)$. (b) Similar experiment with a weak modulation $\epsilon_\mathrm{m} = \frac{1}{25}\Omega, \theta_\mathrm{m} = 0$. Note that the signal contrast of a normal Rabi oscillation measured in our sample is around 1%–2%.

combination of the spin precession, at a rate ϵ_m, and the rotating frame transformation with frequency ω_m, yielding the two sidebands $\omega_\mathrm{m} \pm \epsilon_\mathrm{m}$. For a generic initial state, all three bands contribute to the signal.

Beyond the RWA, higher order frequency components as well as frequency and amplitude shifts complicate the dynamics. Still, their effects can be precisely predicted by Floquet theory [31]. Since frequency shifts of the Mollow triplet due to strong driving are still small even when $\epsilon_\mathrm{m} \approx \Omega$ [31], we assume that the RWA of the second rotating frame is valid when analyzing the coherence time in section 3 for each band.

The two sidebands are affected by fluctuations of the second driving field, whereas the center band frequency is robust against noise, as it depends only on the modulation frequency which is set with high precision. Thus, while a generic, *unknown* state coherence is limited by the shorter, sideband coherence, we can use our knowledge of the central band dynamics to better protect a *known*, arbitrary state, by synchronizing the mode of the center band to the qubit state. To demonstrate these improvements, in experiments we evaluate the coherence improvement of the center band and sidebands separately, by setting different modulation phases and initial states. First, we show in figure 1(c) that the coherence of the sidebands displays a large improvement by more than an order of magnitude, when compared to a normal Rabi oscillation. By further tuning the parameters $\phi_0, \theta_\mathrm{m}$ in the CCD scheme, we can orient the driving field in the second rotating frame along the direction of the initial state to be protected. This synchronizes the state evolution to the Mollow center band, and achieves a 500-fold improvement in the coherence time, compared to the conventional Rabi oscillations. Figure 1(e) shows the coherence of two different initial states synchronized to the center band. In the upper panel, the initial state is $|0\rangle$ and the driving phases are $\phi_0 = 0, \theta_\mathrm{m} = 0$; in the lower panel, the initial state is $\cos\left(\frac{\pi}{8}\right)|0\rangle + \mathrm{e}^{\mathrm{i}\frac{\pi}{4}}\,\sin\left(\frac{\pi}{8}\right)|1\rangle$ and the driving phases are $\phi_0 = -\frac{\pi}{4}, \theta_\mathrm{m} = \frac{\pi}{4}$. Note that the coherence times of both states are similar, indicating that an arbitrary known state can be protected.

To understand the source of the mode-synchronized driving robustness we first analyze the effects of static inhomogeneities in the driving and static fields, before considering a more general noise model in the next section. In addition to providing a more intuitive picture, inhomogeneities are often a main source of decoherence when manipulating large ensemble of spins. We measure the Rabi oscillations from $t = 50\ \mu$s to $t = 50.5\ \mu$s to ensure that only the center band has survived, and extract the oscillation contrast c_1 by fitting the signal to $c_0 + \frac{1}{2}c_1\,\cos(\omega_1 t + \phi_1)$. In figure 2, we compare the results with a strong (a) and weak (b) modulation strength ϵ_m. In the first case, the center band has a large amplitude in a broader region beyond the resonance condition $\sqrt{\Omega^2 + \delta^2} = \omega_\mathrm{m}$, showing that more spins are driven even if their detuning and Rabi frequency deviates from the nominal ones due to inhomogeneities. Another evidence of robustness is that the measured oscillation contrast (intensity in the color map) at a nominal $\delta = 0, \Omega = \omega_\mathrm{m}$ under strong modulation is larger than that under weak modulation, indicating that the strong modulation improves the protection of the center band coherence. The improvement under strong modulation can be intuitively understood by considering the Hamiltonian in the second rotating frame with $\phi_0 = 0, \theta_m = 0, H_I^{(2)} = \frac{\Omega_R - \omega_m}{2}\sigma'_x + \frac{\epsilon_m}{2}\sigma'_z$ where $\sigma'_x = \frac{\Omega}{\Omega_R}\sigma_x - \frac{\delta}{\Omega_R}\sigma_z, \sigma'_z = \frac{\Omega}{\Omega_R}\sigma_z + \frac{\delta}{\Omega_R}\sigma_x$. Stronger driving will set $\omega_m \approx \Omega_R$ (reducing static field inhomogenities) and strong modulation ϵ_m will reduce the effects of the first driving (Ω) inhomogeneity, with the width of the intense region in figure 2 on the order of modulation strength ϵ_m. A precise simulation by Floquet theory and more discussions on the strong driving effects are in appendix A. Further insight on the protection given by a larger modulation can be obtained by analyzing a more complete model that includes the noise spectrum dependence of the coherence time of both the center band and the sidebands (see section 3).

We note that similar order-of-magnitude improvements in the qubit coherence had only been observed for single NV centers [20], or for small ensembles of NVs [24, 30], while here we are able to engineer robust control over a large volume consisting of an ensemble of 10^{10} NV spins. In addition, we identified the mechanism for robust protection of known quantum states via mode control, that was only previously achieved with mechanical driving [28].

3. Coherence time analysis

To further understand the protection afforded by the CCD scheme, as well as select the optimal driving parameters, it is critical to develop a theoretical framework for the coherence time of qubit ensembles under this scenario, and implement experiments to verify the theoretical predictions.

In the regime of a qubit weakly coupled to the bath, its decay rate under a single transverse driving field can be predicted by the GBE where the relaxation rates are given by the spectral components of the noise on resonance with the corresponding transition energies of the qubit [39]. The coherence time of the qubit is thus determined by the power spectral density (PSD) of the noise [40, 41]. Here we generalize the GBE model to an ensemble of spins, modeling the ensemble as a single spin qubit, where field inhomogeneities are included as an additional zero-frequency component in the noise spectrum. With a semi-classical treatment, the field fluctuations can be included as a stochastic component in the amplitude-modulated CCD Hamiltonian, yielding

$$H = \frac{\omega_0}{2}\sigma_z + (\Omega + \xi_\Omega)\cos(\omega t)\sigma_x + 2(\epsilon_m + \xi_{\epsilon_m})\sin(\omega t)\sin(\omega_m t - \theta_m)\sigma_x + \xi_x\sigma_x + \xi_z\sigma_z \qquad (5)$$

where ξ_Ω, ξ_{ϵ_m} are the fluctuations of the driving fields, comprising both driving fluctuations and inhomogeneities. ξ_x, ξ_z are the fluctuations of the transverse and longitudinal field giving rise to T_1 and T_2 decay in the absence of driving, with contributions from both the bath and the static field inhomogeneities. Assuming stationary processes, the time correlation of these fluctuations is the Fourier transformation of their noise PSD, $\langle \xi_j(t_1)\xi_j(t_2)\rangle = \frac{1}{2\pi}\int_{-\infty}^{\infty} d\nu S_j(\nu) e^{-i\nu(t_2-t_1)}$ where $S_j(\nu)(j = x, z, \Omega, \epsilon_m)$ is the PSD of the corresponding noise in the lab frame. In the same way we can better understand the unitary dynamics by applying rotating frame transformations to the Hamiltonian, here we can analyze the noise effects and derive the expected decay rates by expressing the PSDs in the rotating frame as a function of the PSDs in the lab frame [39–41]. This is important as only some frequency components of the PSD contribute mostly to the decay in any given frame: the transverse on-resonance noise component contributes to the qubit random bit flips, whereas the longitudinal noise components at zero frequency contribute to random phase flips.

For a single driving field ($\epsilon_m = \xi_{\epsilon_m} = 0$) and under the resonance condition $\omega = \omega_0$, the longitudinal and transverse relaxation times in the first rotating frame, $T_{1\rho}$, $T_{2\rho}$, are

$$\frac{1}{T_{1\rho}} = \frac{1}{2}S_x(\omega_0) + S_z(\Omega) = \frac{1}{2T_1} + S_z(\Omega) \qquad (6)$$

$$\frac{1}{T_{2\rho}} = \frac{1}{2T_{1\rho}} + \frac{1}{2}S_x(\omega_0) + \frac{1}{4}S_\Omega(0). \qquad (7)$$

Given long T_1 relaxation times, the longitudinal relaxation $T_{1\rho}$, corresponding to the spin-locking condition, is dominated by $S_z(\Omega)$, the longitudinal field fluctuations. For a zero-frequency centered noise spectrum, larger driving strengths Ω result in better coherence as $S_z(\Omega)$ picks the noise at a frequency farther away from zero. The transverse relaxation time $T_{2\rho}$ describes the decay of a conventional Rabi oscillation. The dominant terms are typically $\frac{1}{2}S_z(\Omega) + \frac{1}{4}S_\Omega(0)$, leading to competing effects as a function of Ω. When Ω is increased, $\frac{1}{2}S_z(\Omega)$ decreases but $\frac{1}{4}S_\Omega(0)$ increases. In figure 3(a), we study the driving strength dependence of the Rabi coherence. Since the coherence time monotonically decreases in the measured range, $\frac{1}{4}S_\Omega(0)$ is the dominant source. When the Rabi driving is off-resonance, the Hamiltonian in the rotating frame has components in the x–z plane. Then, the transverse decay rate includes a term $\propto \frac{\delta^2}{\Omega^2+\delta^2}S_z(0)$ (see details in appendix D) that soon dominates since it probes the spectrum at zero

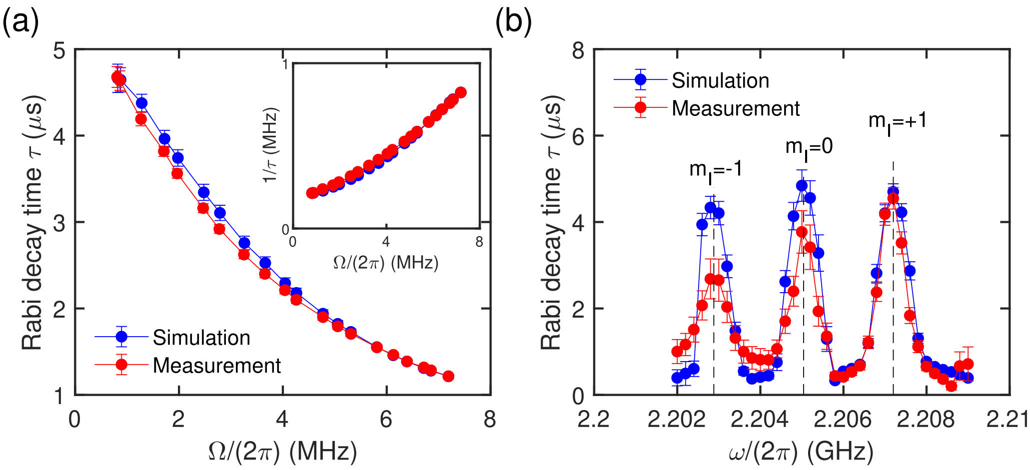

Figure 3. Inhomogeneity characterization. (a) Power dependence of the Rabi coherence time $T_{2\rho}$. Microwave frequency $\omega = \omega_0 = (2\pi)2.2072$ GHz is on resonance with the $|m_I = +1\rangle$ sublevel of nuclear spin of ^{14}N. (b) Detuning dependence of the Rabi coherence time $T_{2\rho}$. Microwave power is chosen such that Rabi frequency under resonance condition is 0.7 MHz. Simulations plotted in blue points are calculated by integrating the Rabi oscillation over power and detuning distributions $f(\Omega + \xi_\Omega, \omega + \xi_z) = \frac{1}{2\pi\sigma_\Omega\sigma_\omega}\exp\left(-\frac{\xi_\Omega^2}{2\sigma_\Omega^2} - \frac{\xi_\omega^2}{2\sigma_\omega^2}\right)$ and summing up the three species of nuclear spin sublevels with the population of each sublevel obtained from the ESR measurement. Values $\sigma_\Omega = 0.016\Omega$ and $\sigma_\omega = (2\pi)0.32$ MHz are used in the simulation. An exponential decay $c_0 + c_1\exp\left(-\frac{t}{\tau}\right)\cos(\omega_1 t + \phi_1)$ is used in the fitting to extract the coherence time τ.

frequency. Thus, the Rabi coherence dependence on the detuning δ provides information about the static field fluctuation $S_z(0)$, and locally optimal coherence is obtained under three resonance frequencies corresponding to three nuclear spin sub-levels. To extract the values of inhomogeneities from the experimental data, we simulate the decay rate with a simple model by directly integrating the Rabi oscillation over a static Gaussian distribution of the driving field inhomogeneities ξ_Ω and static field inhomogeneities ξ_z. The optimal fit to experiments is obtained with parameters $\sigma_\Omega \sim 1.6\%\Omega$ and $\sigma_\omega = 4S_z(0) = (2\pi)0.32$ MHz, or $\sigma_\omega \approx 0.015\%\omega$.

We can extend this analysis to the CCD protocol by entering a second rotating frame. On resonance $\omega_m = \Omega$, we obtain the longitudinal and transverse relaxation times $T_{1\rho\rho}$, $T_{2\rho\rho}$ in the second rotating frame,

$$\frac{1}{T_{1\rho\rho}} = \frac{1}{4}S_\Omega(\epsilon_m) + \frac{3}{4}S_x(\omega_0) + \frac{1}{4}[S_z(\Omega - \epsilon_m) + S_z(\Omega + \epsilon_m)] \tag{8}$$

$$\begin{aligned}\frac{1}{T_{2\rho\rho}} &= \frac{1}{2T_{1\rho\rho}} + \frac{1}{4}S_{\epsilon_m}(0) + \frac{1}{2}S_z(\Omega) + \frac{1}{4}S_x(\omega_0)\\ &= \frac{1}{4}S_{\epsilon_m}(0) + \frac{1}{8}S_\Omega(\epsilon_m) + \frac{1}{2}S_z(\Omega) + \frac{1}{8}[S_z(\Omega - \epsilon_m) + S_z(\Omega + \epsilon_m)] + \frac{5}{8}S_x(\omega_0)\end{aligned} \tag{9}$$

$T_{1\rho\rho}$ is the coherence time under the spin-locking condition in the second rotating frame, which corresponds to the center band in the Mollow triplet. $T_{2\rho\rho}$ is the coherence time for the sidebands. By analyzing the dominant noise sources, we can explain the decay rates observed in experiments, as shown in figure 4, and propose good control strategies.

The coherence time $T_{1\rho\rho}$ shows a strong dependence on the driving powers, ϵ_m. The fast initial increase in coherence time is due to the fast decrease of $S_\Omega(\epsilon_m)$ as ϵ_m grows, followed by a broad plateau. When ϵ_m approaches Ω, a fast decrease happens in the coherence time as observed in figure 4(b) due to the increase of the noise term $\frac{1}{4}S_z(\Omega - \epsilon_m)$ around zero frequency. The values of the optimal coherence time $T_{1\rho\rho}$ in both (a) and (b) approach the spin-locking coherence $T_{1\rho}$ under the same driving strength Ω (see details in figure 7 in appendix D), which verifies that the coherence of both the spin-locking condition and the center band in the CCD scheme is dominated by S_z. This result points to a strategy to improve the spin-locking coherence time under CDD, by increasing the second drive strength past the first, $\epsilon_m > \Omega$. We note that in this regime, high-order Floquet effects need to be taken into account [31]. Since no S_{ϵ_m} term is involved in the center band coherence, phase modulation and amplitude modulation do not display a significant difference.

The coherence time for the sidebands $T_{2\rho\rho}$ also shows a maximum as a function of ϵ_m. This is due to the competing effects of $\frac{1}{8}S_\Omega(\epsilon_m) + \frac{1}{8}S_z(\Omega + \epsilon_m)$, which decreases with increasing ϵ_m and $\frac{1}{4}S_{\epsilon_m}(0) + \frac{1}{8}S_z(\Omega - \epsilon_m)$,

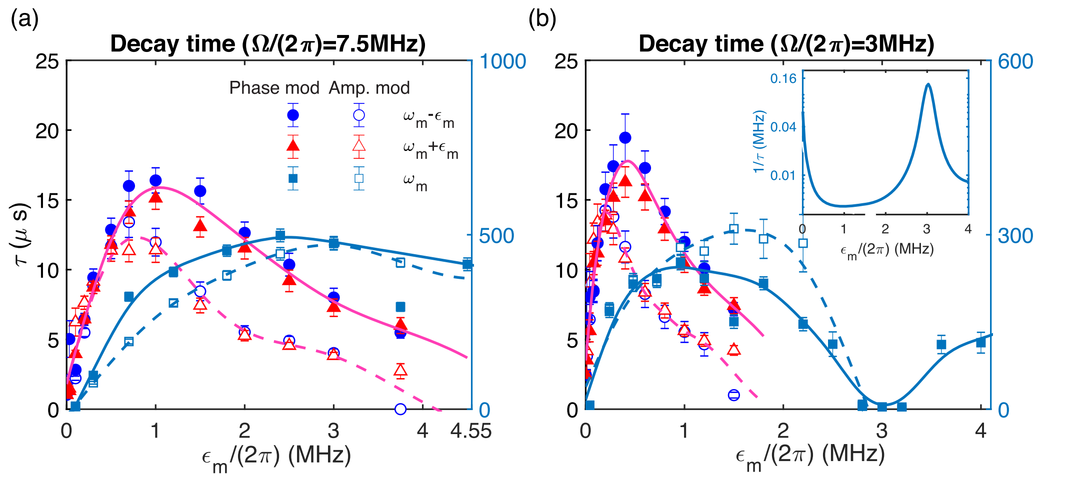

Figure 4. (a) Coherence times $T_{1\rho\rho}$, $T_{2\rho\rho}$ as a function of ϵ_m. Parameters $\omega_m = \Omega = (2\pi)7.5$ MHz, $\delta = 0$, and initial state is prepared to $|0\rangle$. Sidebands coherence times are plotted in red points for $\omega_m + \epsilon_m$ and blue points for $\omega_m - \epsilon_m$. Center band coherence times are plotted in light blue points. Solid points and curves are for phase modulation whereas hollow points and dashed lines are for amplitude modulation. Two y axes are used for sidebands (left) and center band (right). (b) Coherence times $T_{1\rho\rho}$, $T_{2\rho\rho}$ dependence on ϵ_m. Parameters $\omega_m = \Omega = (2\pi)3$ MHz. The inset is the decay rate $1/\tau$ of the center band under the phase modulation condition.

which instead increases. Since $\frac{1}{4}S_{\epsilon_m}(0)$ always picks up the DC noise components, it soon dominates when ϵ_m keeps increasing, so that the coherence degradation happens earlier than for the center band. Characterizing the various noise spectrum components can inform the best driving parameters for optimal coherence.

For an ideal situation of phase modulation, we should have $\xi_{\epsilon_m} = 0$, $\frac{1}{4}S_{\epsilon_m}(0) = 0$, and the decrease of coherence time $T_{2\rho\rho}$ should only be induced by the $\frac{1}{8}S_z(\Omega - \epsilon_m)$ term, predicting a coherence time close to $T_{1\rho\rho}$. However, both previous experiments [24] and this work do not find significant difference between phase modulation and amplitude modulation, although indeed the maximum is shifted toward higher ϵ_m. In both strong power and weak power cases in figures 4(a) and (b) respectively, the phase modulation only shows a slight improvement for the sidebands and the coherence time of the sidebands is 1–2 orders of magnitude smaller than the center band. The noise ξ_{ϵ_m} under the phase modulation may come from the phase noise of the microwave field.

4. Conclusion

In this work, we explore optimal coherence protection by the CCD technique in dense NV ensembles. We show that any arbitrary states can be protected by aligning the driving field with the state to be protected, thus engineering a single mode evolution that corresponds to the center band in the Mollow triplet. Our experiments show that such a technique can be used to synchronize the dynamics of qubit ensembles even in the presence of large inhomogeneity. We generalize the GBE to include driving fluctuations and to analyze the coherence under the CCD protocol. By experimentally measuring the dependence of the coherence time on the second driving strength ϵ_m, we can validate our theoretical analysis and analyze the interplay of competing noise sources. In addition to providing a useful tool for protecting known and unknown quantum states, the insights into the CCD dynamics have found applications in high-frequency AC magnetic field sensing [42, 43]. The robust driving of the NV center ensemble could further enable the indirect protection of the ^{14}N nuclear spin associated with the NV center, whose coherence is limited by the random telegraph noise caused by the T_1 relaxation of the NV electronic spin. The nuclear spin protection requires rapid flips of the NV electron spin [44], which can be accomplished by the CCD scheme. Similarly, robust driving of the electronic spin bath [34], could enhance the NV coherence time. Finally, the scheme demonstrated in this work can be used to design robust quantum control pulses [21].

Acknowledgments

This work was supported in part by DARPA DRINQS and NSF PHY1915218. We thank Pai Peng for fruitful discussions and Thanh Nguyen for manuscript revision.

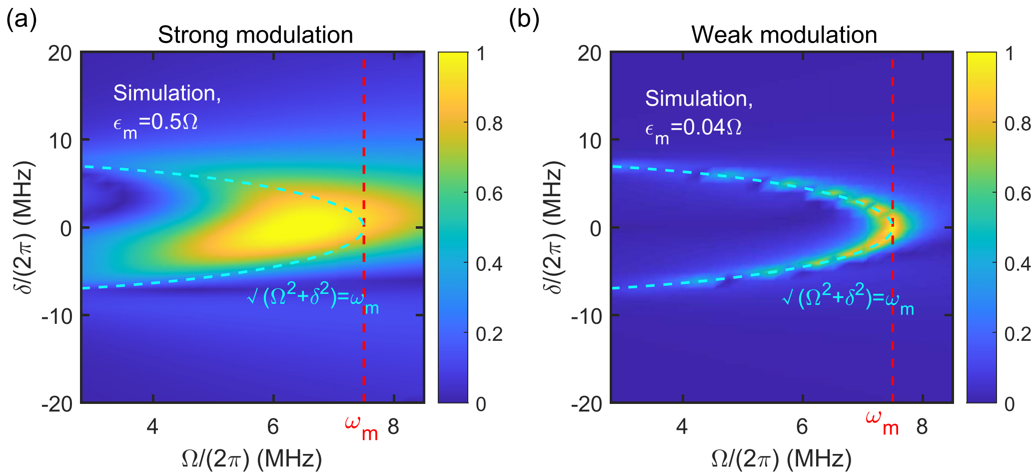

Figure 5. Floquet simulation for the experiment in figure 2. The oscillation contrast of the center band is calculated assuming a single NV under the same driving condition as in the experiment seen in figure 2. The decay effects caused by the noise are taken into account by only keeping the initial contrast of the center band while neglecting the contrast contributed from the sidebands in the simulation. The intensity of the colormap represents the contrast value. Under the optimum driving condition, the maximum contrast (=1) is achieved. Please see reference [31] for details on the Floquet simulation.

Appendix A. Dynamics of the CCD scheme

To predict the precise dynamics of the CCD scheme, we utilize Floquet theory to simulate the evolution. The eigenvectors of a time-periodic Hamiltonian are given by $\mathrm{e}^{-\mathrm{i}\lambda^a t}\Phi^a(t)$ where $\{\lambda^a\}$ are the eigen-energies, and $\Phi^a(t) = \Phi^a(t+T)$ are periodic in time, with $T = \frac{2\pi}{\omega_\mathrm{m}}$. The evolution of an arbitrary qubit state can then be written as $\Psi(t) = c^+\,\mathrm{e}^{-\mathrm{i}\lambda^- t}\Phi^+(t) + c^-\,\mathrm{e}^{-\mathrm{i}\lambda^+ t}\Phi^-(t)$ with the coefficients $c^\pm$ set by the initial conditions. If the initial state is one of the two eigenstates $\Phi^\pm(0)$, then the spin-locking condition is satisfied and the state evolution will only involve one mode, associated with the corresponding $\lambda^\pm$. The Rabi oscillations will only include frequency components that are integer multiples of ω_m. Otherwise, the evolution will be a superposition of these two modes, and the Rabi oscillations will involve three sets of frequencies, $n\omega_\mathrm{m}$ and $n\omega_\mathrm{m} \pm (\lambda^+ - \lambda^-)$. By tuning the driving parameters, the evolution mode can be well controlled.

In the presence of inhomogeneities of the first drive, a stronger modulation is needed to synchronize more ensemble spins to the center band evolution. In the main text (figure 2), we experimentally measured the power and detuning dependence of the center band oscillation contrast (twice the oscillation amplitude) under strong and weak modulation strengths ϵ_m. In figure 5, we use Floquet theory to calculate the center band oscillation contrast of a single NV under the experimental conditions, and find a good match with the experiment results. On resonance $\omega_\mathrm{m} = \Omega, \delta = 0$, the simulation predicts similar contrast for both strong and weak modulation. However, in the experiments in figure 2 we found that the oscillation contrast was larger with the strong modulation. This can be easily understood by considering that even under a nominal resonance condition, many spins in the ensemble have an offset, due to inhomogeneities, and only a strong drive is enough to achieve a good control. In figure 6, we plot 1D cuts of both the experimental data (symbols) and results obtained from simulation (curves). Under strong modulation, the oscillation amplitude as a function of detuning has a full width at half maximum much larger than the hyperfine coupling constant $A = 2.2$ MHz between NV electronic spin and ^{14}N nuclear spin. This indicates that we can effectively synchronize all nuclear spin sublevels to the center band, and thus protect a known NV state irrespective of the nuclear state.

The performance of the center band protection is analyzed in detail in section 3 with the noise spectrum analysis, where we show that a modulation strength $\epsilon_\mathrm{m} \approx \frac{1}{2}\Omega$ results in less decay effects and better coherence times than the case with $\epsilon_\mathrm{m} \ll \Omega$. Here we provide another qualitative intuition of the performance comparison with a simple model assuming the validity of the RWA. We assume $\phi_0 = 0, \theta_\mathrm{m} = 0$, and the initial state is $|0\rangle$ for the amplitude-modulated CCD scheme. When $\delta = 0$, the Hamiltonian in the second rotating frame is $\frac{\Omega-\omega_\mathrm{m}}{2}\sigma_x + \frac{\epsilon_\mathrm{m}}{2}\sigma_z$. Under the resonance condition $\Omega = \omega_\mathrm{m}$, the initial state is in the same direction as the static field in the second rotating frame, thus the 'spin-locking' condition is satisfied and the amplitude of the center band is the maximum. When $\frac{|\Omega-\omega_\mathrm{m}|}{\epsilon_\mathrm{m}} \gg 1$, the initial state becomes perpendicular to the static field, and the center band is vanishing. Similar analysis applies to the detuning dependence. As a result, the width of the intense region in figures 2 and 5 is on the order of

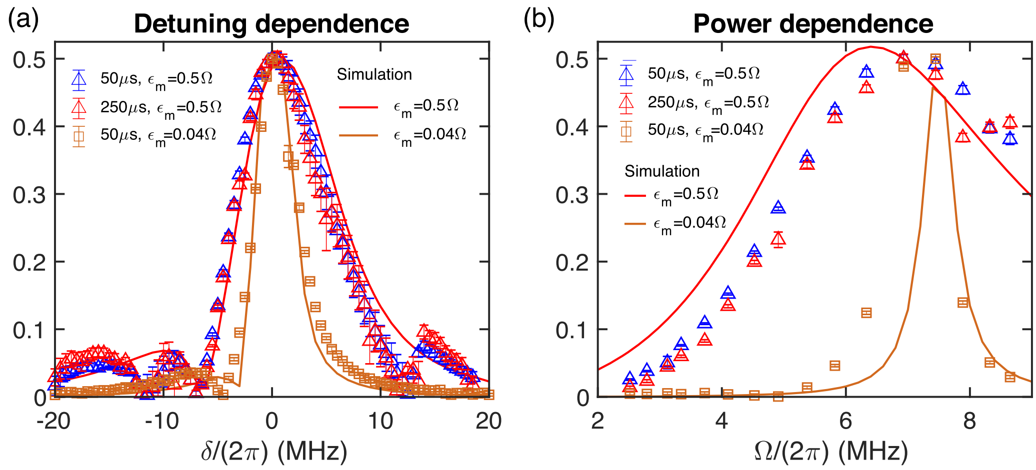

Figure 6. 1D cuts of robustness experiments in figure 2 and simulations in figure 5. (a) Detuning δ dependence of center band amplitude, which is a cut of the intensity plot in figure 2(a) along $\Omega = (2\pi)7.5$ MHz. Blue triangles and red triangles are data of Rabi oscillation coefficients fitted from Rabi oscillations at time 50 μs (from 50 μs to 50.5 μs) and 250 μs (from 250 μs to 250.25 μs) correspondingly under strong modulation $\epsilon_{\mathrm{m}} = \frac{1}{2}\Omega, \theta_{\mathrm{m}} = 0$. Yellow squares are data at time 50 μs with weak modulation $\epsilon_{\mathrm{m}} = \frac{1}{25}\Omega, \theta_{\mathrm{m}} = 0$. Red and yellow curves are theoretical prediction of Floquet theory. (b) Power dependence of the oscillation coefficients which is a cut of the intensity plots along $\delta = 0$. The colors correspond to those in (a). Note that the plots in (a) and (b) are manually normalized by their maximum value for easier comparison of the peak width, thus the y axis has an arbitrary scale.

Table 1. Comparison of Rabi coherence protection with CCD in NV systems. Note that in [28] and this work, coherence times for different frequency components are discussed separately while all the other work only discuss an overall coherence time.

Parameters	Reference [20] (2012)	Reference [24] (2017)	Reference [28] (2017)	Reference [30] (2020)	This work
Sample	Single NV	NV ensemble (10^4 spins)	Single NV	Nano diamond	NV ensemble (10^{10} spins)
T_1	1.5 ms	5.9 ms	5.1 ms	0.087 35 ms	2.4 ms
$\Omega/(2\pi)$, $T_{2\rho}^*$	40 MHz, 2.3 μs	9 MHz, 0.81 μs	5.83 MHz, 5.3 μs	8.06MHz	7.5 MHz, 1 μs
$\sigma_\Omega/(2\pi)$	~0.1 MHz	~0.07MHz	~0.2 MHz	~0.1 MHz	~0.2 MHz
$\epsilon_{\mathrm{m}}/(2\pi)$	~1 MHz	~1 MHz	~4.1 MHz	~0.1 MHz	3 MHz, 1 MHz
$T_{1\rho\rho}$			~2.9 ms		~0.5 ms
$T_{2\rho\rho}$	21 μs	~14 μs	~100 μs	~30 μs	~15 μs

the modulation strength ϵ_{m}, and larger ϵ_{m} results in better robustness against power and detuning fluctuations. Nevertheless, under the strong driving condition, the optimal Ω shifts from the resonance position ω_{m} predicted by the RWA. This effect cannot be analytically predicted by the RWA and the Floquet theory is needed as a more precise simulation tool. Detailed exploration about the amplitude shifts due to strong driving effect is reported in reference [31].

Appendix B. Comparison to previous works

Table 1 makes a comparison of our work to previous ones. An order of magnitude coherence improvement was achieved in both single NV [20] and sparse NV ensembles [24] by applying the CCD scheme with resonant microwave, and the CCD scheme was also able to improve the coherence of NVs in nano diamonds [30]. The CCD scheme has also been explored by combining high quality mechanical driving, serving as the modulation field, and microwave driving [28]; the coherence of a single NV was improved by one order of magnitude. In comparison, we achieve a 15-fold improvement for the coherence of the two sidebands in a large volume of NV ensembles with 10^{10} spins. In addition, we also observe a 500-fold improvement for the central band at ω_{m}, whose long coherence was only previously identified in the mechanical driving experiment. While the latter achieved a similar coherence enhancement, using microwaves only further allows the implementation of mode control of the evolution, and the phase-modulated CCD scheme can generate larger modulation strength without being limited by microwave power, which provides a more flexible tool for finding optimal coherence and generating even more applications.

Appendix C. Inhomogeneity characterization

To characterize the inhomogeneity in our sample, we study the power and detuning dependence of the Rabi coherence. Assuming that inhomogeneities in the driving power and static field are the two main sources of decay for the Rabi oscillations, we simulate the coherence time. We assume a Gaussian distribution of their values, $f(\Omega+\xi_\Omega,\omega+\xi_\omega)=\frac{1}{2\pi\sigma_\Omega\sigma_{\xi_z}}\ \exp\left(-\frac{\xi_\Omega^2}{2\sigma_\Omega^2}-\frac{\xi_\omega^2}{2\sigma_\omega^2}\right)$, where ξ_Ω describes the driving strength inhomogeneity and ξ_ω the static field along the z axis. We take the inhomogeneity of the drive to be proportional to the driving amplitude, $\xi_\Omega=r_\Omega\cdot\Omega$, where ξ_ω is fixed. Rabi oscillations are simulated by a two-dimensional integration over the power and detuning inhomogeneity

$$P_{|0\rangle}(t)=\sum_{i=1}^{3}\frac{1}{2}c_i\int_{-\infty}^{\infty}\int_{-\infty}^{\infty}\mathrm{d}\xi_\Omega\,\mathrm{d}\xi_\omega f(\Omega+\xi_\Omega,\omega+\xi_\omega)\frac{\Omega}{\sqrt{\Omega^2+(\omega-\omega_i)^2}}\cos\left(\sqrt{\Omega^2+(\omega-\omega_i)^2}t\right)\mathrm{e}^{-t/\tau_0}$$

In figure 3 of the main text, we plot the simulation results (blue points) when varying the Rabi amplitude and resonance frequency. By comparing the dependence of the simulation results on these parameters under our control with the experiments, we obtain an estimate of the inhomogeneity distribution, $\sigma_\Omega=0.016\Omega$ and $\sigma_\omega=(2\pi)0.32$ MHz. In simulations, we find that the slope of the Ω-dependence (figure 3(a)) is more sensitive to the driving inhomogeneity σ_Ω, while the peak width as a function of ω (figure 3(b)) is more sensitive to the static field variance, σ_ω, which can be explained with the theory in appendix D. To make the simulation best fit the experiment, we choose an intrinsic coherence time $\tau_0=13\ \mu$s, which gives a constant offset to the decay rates and may come from other noise sources, such as the spin bath.

Appendix D. Coherence limit

To analyze the effect of noise on the spin coherence, we consider a semiclassical model, where the noise is taken to be a fluctuating field originating from a classical bath. Introducing these stochastic components and assuming $\phi_0=0$, the amplitude-modulated CCD Hamiltonian reads

$$H=\frac{\omega_0}{2}\sigma_z+(\Omega+\xi_\Omega)\cos(\omega t)\sigma_x+2(\epsilon_\mathrm{m}+\xi_{\epsilon_\mathrm{m}})\sin(\omega t)\sin(\omega_\mathrm{m}t-\theta_\mathrm{m})\sigma_x+\xi_x\sigma_x+\xi_z\sigma_z \tag{D.1}$$

where ξ_x,ξ_z are the fluctuations of the effective transverse and longitudinal fields and ξ_Ω, $\xi_{\epsilon_\mathrm{m}}$ are the fluctuations of the driving field. Within the RWA, $\Omega\ll\omega$, the Hamiltonian in the first rotating frame is

$$H_\mathrm{I}^{(1)}=\left[-\frac{\delta}{2}+\xi_z\right]\sigma_z+\left[\frac{\Omega+\xi_\Omega}{2}+\xi_x\ \cos(\omega_0t)\right]\sigma_x+\left[-(\epsilon_\mathrm{m}+\xi_{\epsilon_\mathrm{m}})\sin(\omega_\mathrm{m}t-\theta_\mathrm{m})-\xi_x\ \sin(\omega_0t)\right]\sigma_y \tag{D.2}$$

where $\delta=\omega-\omega_0$ is the resonance offset. In the following, we will analyze four cases based on this model: on-resonance single driving, off-resonance single driving, amplitude-modulated CCD, and phase-modulated CCD.

D.1. Single driving with $\delta=0$

We first analyze the case without the second driving with $\epsilon_\mathrm{m}=0$ and compare with previous work in reference [39]. The PSDs in the first rotating frame $S_j^{(1)}$ can be expressed as a function of the PSDs in the lab frame

$$\begin{aligned}S_x^{(1)}(\nu)&=\frac{1}{4}S_\Omega(\nu)+\frac{1}{4}\left[S_x(\nu+\omega_0)+S_x(\nu-\omega_0)\right]\\S_y^{(1)}(\nu)&=\frac{1}{4}\left[S_x(\nu+\omega_0)+S_x(\nu-\omega_0)\right]\\S_z^{(1)}(\nu)&=S_z(\nu)\end{aligned} \tag{D.3}$$

We can write the decay rates Γ_α of the $\alpha=\{x,y,z\}$ components of the qubit Pauli matrix as

$$\begin{aligned}\Gamma_x&=\frac{1}{4}\left[S_x(\omega_0+\Omega)+S_x(\omega_0-\Omega)\right]+S_z(\Omega)\\\Gamma_y&=\frac{1}{2}S_x(\omega_0)+S_z(\Omega)+\frac{1}{4}S_\Omega(0)\\\Gamma_z&=\frac{1}{2}S_x(\omega_0)+\frac{1}{4}\left[S_x(\omega_0+\Omega)+S_x(\omega_0-\Omega)\right]+\frac{1}{4}S_\Omega(0)\end{aligned} \tag{D.4}$$

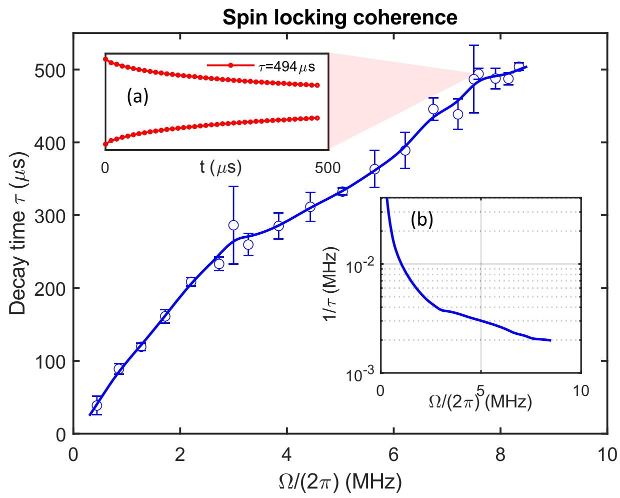

Figure 7. Spin-locking coherence time τ as a function of the driving strength $\Omega/(2\pi)$. After initializing the qubit to $|0\rangle$ state, a $\frac{\pi}{2}$ pulse along the y axis rotates the spin to $\frac{1}{\sqrt{2}}(|0\rangle + |1\rangle)$, then an on-resonance transverse driving field is applied continuously for a time interval, finally a $\frac{\pi}{2}$ pulse along the $y(-y)$ axis is applied to flip the spin to $-z(z)$ direction for population measurement in $|0\rangle$. By measuring the population in $|0\rangle$ while varying the time intervals between two $\frac{\pi}{2}$ pulses, the spin-locking coherence time can be extracted. Inset (a) is the data plot for $\Omega = (2\pi)7.5$ MHz. Inset (b) is the decay rate $\frac{1}{\tau}$ as a dependence of the driving strength $\Omega/(2\pi)$.

where we used the fact that the decay along one axis is determined by the sum of the rotating frame spectra along the two other axes, $\Gamma_\alpha = S_\beta^{(1)} + S_\gamma^{(1)}$. In turn, these rates can be used to write the longitudinal and transverse relaxation time in the first rotating frame $T_{1\rho}$, $T_{2\rho}$. With the approximation $S_x(\omega_0 \pm \Omega) \approx S_x(\omega_0)$, we obtain

$$\begin{aligned}\frac{1}{T_{1\rho}} &= \Gamma_x = \frac{1}{2}S_x(\omega_0) + S_z(\Omega)\\ \frac{1}{T_{2\rho}} &= \frac{1}{2}(\Gamma_y + \Gamma_z) = \frac{3}{4}S_x(\omega_0) + \frac{1}{2}S_z(\Omega) + \frac{1}{4}S_\Omega(0) = \frac{1}{2T_{1\rho}} + \frac{1}{T'_{2\rho}}\end{aligned} \tag{D.5}$$

where we defined the pure dephasing time $T_{2\rho'}$ with $\frac{1}{T'_{2\rho}} = \frac{1}{2}S_x(\omega_0) + \frac{1}{4}S_\Omega(0) = \frac{1}{2T_1} + \frac{1}{4}S_\Omega(0)$. Our analysis up to here is consistent with previous work in reference [39] except for an additional microwave fluctuation term. Figure 7 is a measurement of spin-locking coherence as a function of Ω. The coherence time increases with Ω due to the decreasing of $S_z(\Omega)$. The inset (b) plots the decay rate and is a direct measurement of $S_z(\Omega)$ [41, 45]. Since the spectrum is concentrated at zero frequency, the static field inhomogeneity is much stronger than other frequency components of the spin bath, which also validates the simplified model we use in the inhomogeneity characterization in appendix C.

D.2. Single driving with $\delta \neq 0$

When there is a frequency offset, $\delta \neq 0$, we can diagonalize the non-stochastic Hamiltonian (in the σ_x basis) by defining a new set of axes in the first rotating frame with $\sigma_z = \frac{\Omega}{\Omega_R}\sigma_{z'} - \frac{\delta}{\Omega_R}\sigma_{x'}, \sigma_x = \frac{\Omega}{\Omega_R}\sigma_{x'} + \frac{\delta}{\Omega_R}\sigma_{z'}$, $\sigma_y = \sigma_{y'}$ where $\Omega_R = \sqrt{\delta^2 + \Omega^2}$ is the effective driving field. Then, the Hamiltonian in the first rotating frame becomes

$$\begin{aligned}H_I^{(1)} &= -\frac{\delta}{2}\sigma_z + \frac{\Omega}{2}\sigma_x - \xi_x\,\sin(\omega_0 t)\sigma_y + \left[\frac{\xi_\Omega}{2} + \xi_x\,\cos(\omega_0 t)\right]\sigma_x + \xi_z\sigma_z\\ &= \frac{\Omega_R}{2}\sigma_{x'} + \xi_z\left[\frac{\Omega}{\Omega_R}\sigma_{z'} - \frac{\delta}{\Omega_R}\sigma_{x'}\right] + \left[\frac{\xi_\Omega}{2} + \xi_x\,\cos(\omega_0 t)\right]\left[\frac{\Omega}{\Omega_R}\sigma_{x'} + \frac{\delta}{\Omega_R}\sigma_{z'}\right] - \xi_x\,\sin(\omega_0 t)\sigma_{y'}.\end{aligned} \tag{D.6}$$

Accordingly, the PSDs in this modified first rotating frame $S_{\alpha'}^{(1)}$ can be expressed as a function of the PSDs in the lab frame as

$$
\begin{aligned}
S_{x'}^{(1)}(\nu) &= \frac{\delta^2}{\Omega_R^2} S_z(\nu) + \frac{\Omega^2}{\Omega_R^2}\left[\frac{1}{4}S_\Omega(\nu) + \frac{1}{4}(S_x(\nu+\omega_0) + S_x(\nu-\omega_0))\right] \\
S_{y'}^{(1)}(\nu) &= \frac{1}{4}\left[S_x(\nu+\omega_0) + S_x(\nu-\omega_0)\right] \\
S_{z'}^{(1)}(\nu) &= \frac{\Omega^2}{\Omega_R^2} S_z(\nu) + \frac{\delta^2}{\Omega_R^2}\left[\frac{1}{4}S_\Omega(\nu) + \frac{1}{4}(S_x(\nu+\omega_0) + S_x(\nu-\omega_0))\right].
\end{aligned}
\tag{D.7}
$$

Similar to what was done above, we can obtain the decay rates of the $\sigma_{\alpha'}$ components and then combine them to obtain the longitudinal and transverse relaxation rates in the rotating frame. With the approximation $S_x(\omega_0 \pm \Omega_R) \approx S_x(\omega_0)$, we obtain

$$
\frac{1}{T_{1\rho}} = \Gamma_{x'} = \frac{1}{2}S_x(\omega_0) + \frac{\Omega^2}{\Omega_R^2}S_z(\Omega_R) + \frac{\delta^2}{\Omega_R^2}\left[\frac{1}{4}S_\Omega(\Omega_R) + \frac{1}{2}S_x(\omega_0)\right] \tag{D.8}
$$

$$
\begin{aligned}
\frac{1}{T_{2\rho}} &= \frac{1}{2}(\Gamma_{y'} + \Gamma_{z'}) \\
&= \frac{\delta^2}{\Omega_R^2}S_z(0) + \frac{\Omega^2}{4\Omega_R^2}\left[S_\Omega(0) + 2S_z(\Omega_R)\right] + \frac{1}{8}\frac{\delta^2}{\Omega_R^2}S_\Omega(\Omega_R) + \left[\frac{3}{4} + \frac{\delta^2}{\Omega_R^2}\right]S_x(\omega_0).
\end{aligned}
\tag{D.9}
$$

This analysis helps explain the experimental results in figure 3(b) where the coherence of Rabi oscillation becomes worse when the detuning increases, due to the $\frac{\delta^2}{\Omega_R^2}S_z(0)$ term in the transverse decay rate $\frac{1}{T_{2\rho}}$. For a spin-locking experiment with detuning, instead, the decay rate $\frac{1}{T_{1\rho}} \approx S_x(\omega_0) = \frac{1}{T_1}$ approaches the T_1 relaxation time when $\delta \to \infty$.

D.3. Amplitude-modulated CCD

To simplify the calculation, we assume $\omega_0 = \omega, \omega_m = \Omega, \phi_0 = 0, \theta_m = \frac{\pi}{2}$ for all the following discussions. We enter into the second rotating frame defined by $\frac{\omega_m}{2}\sigma_x$ and drop the counter-rotating terms of the driving field but keep the counter-rotating terms of the noise field. The Hamiltonian in the second rotating frame is

$$
\begin{aligned}
H_I^{(2)} =& \frac{\epsilon_m}{2}\sigma_y + \left[\frac{\xi_\Omega}{2} + \xi_x\cos(\omega_0 t)\right]\sigma_x + \left[\frac{\xi_{\epsilon_m}}{2}(1+\cos(2\omega_m t)) - \xi_x\sin(\omega_0 t)\cos(\omega_m t) + \xi_z\sin(\omega_m t)\right]\sigma_y \\
&+ \left[-\frac{\xi_{\epsilon_m}}{2}\sin(2\omega_m t) + \xi_x\sin(\omega_0 t)\sin(\omega_m t) + \xi_z\cos(\omega_m t)\right]\sigma_z.
\end{aligned}
\tag{D.10}
$$

The PSDs in the second rotating frame $S_j^{(2)}$ become

$$
\begin{aligned}
S_x^{(2)}(\nu) =& \frac{1}{4}S_\Omega(\nu) + \frac{1}{4}\left[S_x(\nu+\omega_0) + S_x(\nu-\omega_0)\right] \\
S_y^{(2)}(\nu) =& \frac{1}{4}S_{\epsilon_m}(\nu) + \frac{1}{16}\left[S_{\epsilon_m}(\nu+2\omega_m) + S_{\epsilon_m}(\nu-2\omega_m)\right] + \frac{1}{4}\left[S_z(\nu+\omega_m) + S_z(\nu-\omega_m)\right] \\
&+ \frac{1}{16}\left[S_x(\nu+\omega_0+\omega_m) + S_x(\nu+\omega_0-\omega_m) + S_x(\nu-\omega_0+\omega_m) + S_x(\nu-\omega_0-\omega_m)\right] \\
S_z^{(2)}(\nu) =& \frac{1}{16}\left[S_{\epsilon_m}(\nu+2\omega_m) + S_{\epsilon_m}(\nu-2\omega_m)\right] + \frac{1}{4}\left[S_z(\nu+\omega_m) + S_z(\nu-\omega_m)\right] \\
&+ \frac{1}{16}\left[S_x(\nu+\omega_0+\omega_m) + S_x(\nu+\omega_0-\omega_m) + S_x(\nu-\omega_0+\omega_m) + S_x(\nu-\omega_0-\omega_m)\right].
\end{aligned}
\tag{D.11}
$$

In the second rotating frame, the static field is along the y axis, and the decay rates can be analyzed in a similar way

$$
\begin{aligned}
\Gamma_x &= S_y^{(2)}(0) + S_z^{(2)}(\epsilon_m) \\
\Gamma_y &= S_x^{(2)}(\epsilon_m) + S_z^{(2)}(\epsilon_m) \\
\Gamma_z &= S_y^{(2)}(0) + S_x^{(2)}(\epsilon_m).
\end{aligned}
\tag{D.12}
$$

Define the longitudinal and transverse relaxation times in the second rotating frame as $T_{1\rho\rho}, T_{2\rho\rho}$. Assume that $S_x(\omega_0 \pm \Omega \pm \epsilon_\mathrm{m}) \approx S_x(\omega_0)$ with $\Omega, \epsilon_\mathrm{m} \ll \omega_0$, then

$$\frac{1}{T_{1\rho\rho}} = \Gamma_y = \frac{1}{4}S_\Omega(\epsilon_\mathrm{m}) + \frac{3}{4}S_x(\omega_0) + \frac{1}{16}\left[S_{\epsilon_\mathrm{m}}(2\Omega - \epsilon_\mathrm{m}) + S_{\epsilon_\mathrm{m}}(2\Omega + \epsilon_\mathrm{m})\right] + \frac{1}{4}\left[S_z(\Omega - \epsilon_\mathrm{m}) + S_z(\Omega + \epsilon_\mathrm{m})\right] \tag{D.13}$$

$$\frac{1}{T_{2\rho\rho}} = \frac{1}{2}(\Gamma_x + \Gamma_z) = \frac{1}{2T_{1\rho\rho}} + \frac{1}{4}S_{\epsilon_\mathrm{m}}(0) + \frac{1}{8}S_{\epsilon_\mathrm{m}}(2\Omega) + \frac{1}{2}S_z(\Omega) + \frac{1}{4}S_x(\omega_0) = \frac{1}{T'_{2\rho\rho}} + \frac{1}{2T_{1\rho\rho}} \tag{D.14}$$

where $\frac{1}{T'_{2\rho\rho}} = \frac{1}{4}S_{\epsilon_\mathrm{m}}(0) + \frac{1}{8}S_{\epsilon_\mathrm{m}}(2\Omega) + \frac{1}{2}S_z(\Omega) + \frac{1}{4}S_x(\omega_0)$ is defined as the pure dephasing rate in the second rotating frame.

With $\epsilon_\mathrm{m} \approx \Omega$ and $S_\Omega(\Omega \pm \epsilon_\mathrm{m}) \approx S_\Omega(\Omega)$, the coherence times in the second rotating frame simplifies to

$$\begin{aligned}\frac{1}{T_{1\rho\rho}} &\approx \frac{1}{4}S_\Omega(\epsilon_\mathrm{m}) + \frac{3}{4}S_x(\omega_0) + \frac{1}{8}S_{\epsilon_\mathrm{m}}(2\Omega) + \frac{1}{2}S_z(\Omega)\\ &= \frac{1}{2T_{1\rho}} + \frac{1}{4}S_\Omega(\epsilon_\mathrm{m}) + \frac{1}{2}S_x(\omega_0) + \frac{1}{8}S_{\epsilon_\mathrm{m}}(2\Omega)\end{aligned} \tag{D.15}$$

$$\frac{1}{T_{2\rho\rho}} \approx \frac{1}{4}S_{\epsilon_\mathrm{m}}(0) + \frac{1}{8}S_\Omega(\epsilon_\mathrm{m}) + \frac{3}{16}S_{\epsilon_\mathrm{m}}(2\Omega) + \frac{3}{4}S_z(\Omega) + \frac{5}{8}S_x(\omega_0). \tag{D.16}$$

When $\epsilon_\mathrm{m} \approx \Omega$, the approximation here is no longer valid and the coherence is dominated by $S_z(\Omega - \epsilon_\mathrm{m})$.

D.4. Phase-modulated CCD

There are two-fold differences in the phase-modulated CCD. First, the modulation amplitude could be assumed in principle to be noise-free, since it arises from the phase modulation that should be very precise, as it depends mostly on the signal source, and not on how it is delivered to the spins. Second, the modulated drive is along the z-direction (instead of the y-direction as it is the case for the amplitude-modulated CCD). In the lab frame, we assume $\phi_0 = 0$ and add fluctuation parameters to the phase-modulated CCD Hamiltonian

$$H = \frac{\omega_0}{2}\sigma_z + (\Omega + \xi_\Omega)\cos\left(\omega t - 2\frac{\epsilon_\mathrm{m}}{\Omega}\sin(\omega_\mathrm{m}t - \theta_\mathrm{m})\right)\sigma_x + \xi_x\sigma_x + \xi_z\sigma_z \tag{D.17}$$

where ξ_x, ξ_z are the fluctuations of the transverse and longitudinal fields and ξ_Ω is the fluctuation of the driving field. With the RWA and resonance condition $\Omega \ll \omega = \omega_0$, we can enter into the first rotating frame where

$$\begin{aligned}H_\mathrm{I}^{(1)} = &\frac{\Omega}{2}\sigma_x + \epsilon_\mathrm{m}\cos(\omega_\mathrm{m}t - \theta_\mathrm{m})\sigma_z + \left[\frac{\xi_\Omega}{2} + \xi_x\cos\left(\omega_0 t - 2\frac{\epsilon_\mathrm{m}}{\Omega}\sin(\omega_\mathrm{m}t - \theta_\mathrm{m})\right)\right]\sigma_x\\ &- \xi_x\sin\left(\omega_0 t - 2\frac{\epsilon_\mathrm{m}}{\Omega}\sin(\omega_\mathrm{m}t - \theta_\mathrm{m})\right)\sigma_y + \xi_z\sigma_z.\end{aligned} \tag{D.18}$$

Assume $\theta_\mathrm{m} = \frac{\pi}{2}, \omega_\mathrm{m} = \Omega$ and then the Hamiltonian in the second rotating frame is

$$\begin{aligned}H_\mathrm{I}^{(2)} = &\frac{\epsilon_\mathrm{m}}{2}\sigma_y + \left[\frac{\xi_\Omega}{2} + \xi_x\cos\left(\omega_0 t + 2\frac{\epsilon_\mathrm{m}}{\Omega}\cos(\omega_\mathrm{m}t)\right)\right]\sigma_x\\ &+ \left[\xi_z\sin(\omega_\mathrm{m}t) - \xi_x\sin\left(\omega_0 t + 2\frac{\epsilon_\mathrm{m}}{\Omega}\cos(\omega_\mathrm{m}t)\right)\cos(\omega_\mathrm{m}t)\right]\sigma_y\\ &+ \left[\xi_z\cos(\omega_\mathrm{m}t) + \xi_x\sin\left(\omega_0 t + 2\frac{\epsilon_\mathrm{m}}{\Omega}\cos(\omega_\mathrm{m}t)\right)\sin(\omega_\mathrm{m}t)\right]\sigma_z.\end{aligned} \tag{D.19}$$

The term $\cos(\omega_0 t + 2\frac{\epsilon_\mathrm{m}}{\Omega}\cos(\omega_\mathrm{m}t))$ or $\sin(\omega_0 t + 2\frac{\epsilon_\mathrm{m}}{\Omega}\cos(\omega_\mathrm{m}t))$ can be approximated by calculating the expansion of $\cos(2\frac{\epsilon_\mathrm{m}}{\Omega}\cos(\omega_\mathrm{m}t))$ or $\sin(2\frac{\epsilon_\mathrm{m}}{\Omega}\cos(\omega_\mathrm{m}t))$ to first order when $\epsilon_\mathrm{m}/\Omega$ is small. For example,

$$\begin{aligned}\cos\left(\omega_0 t + 2\frac{\epsilon_\mathrm{m}}{\Omega}\cos(\omega_\mathrm{m}t)\right) &= \cos(\omega_0 t)\cos\left(2\frac{\epsilon_\mathrm{m}}{\Omega}\cos(\omega_\mathrm{m}t)\right) - \sin(\omega_0 t)\sin\left(2\frac{\epsilon_\mathrm{m}}{\Omega}\cos(\omega_\mathrm{m}t)\right)\\ &\approx \cos(\omega_0 t) - \sin(\omega_0 t)2\frac{\epsilon_\mathrm{m}}{\Omega}\cos(\omega_\mathrm{m}t).\end{aligned} \tag{D.20}$$

The PSDs in the second rotating frame $S_j^{(2)}$ become

$$
\begin{aligned}
S_x^{(2)}(\nu) \approx{}& \frac{1}{4}S_\Omega(\nu) + \frac{1}{4}\left[S_x(\nu+\omega_0) + S_x(\nu-\omega_0)\right] + \frac{1}{4}\left(\frac{\epsilon_\mathrm{m}}{\Omega}\right)^2 \left[S_x(\nu+\omega_0+\omega_\mathrm{m}) + S_x(\nu+\omega_0-\omega_\mathrm{m})\right.\\
&\left.+ S_x(\nu-\omega_0+\omega_\mathrm{m}) + S_x(\nu-\omega_0-\omega_\mathrm{m})\right]\\
S_y^{(2)}(\nu) \approx{}& \frac{1}{4}\left[S_z(\nu-\omega_\mathrm{m}) + S_z(\nu+\omega_\mathrm{m})\right] + \frac{1}{16}\left[S_x(\nu+\omega_0+\omega_\mathrm{m}) + S_x(\nu+\omega_0-\omega_\mathrm{m}) + S_x(\nu-\omega_0+\omega_\mathrm{m})\right.\\
&\left.+ S_x(\nu-\omega_0-\omega_\mathrm{m})\right] + \frac{1}{4}\left(\frac{\epsilon_\mathrm{m}}{\Omega}\right)^2 \left[S_x(\nu+\omega_0) S_x(\nu-\omega_0)\right] + \frac{1}{16}\left(\frac{\epsilon_\mathrm{m}}{\Omega}\right)^2 \left[S_x(\nu+\omega_0+2\omega_\mathrm{m})\right.\\
&\left.+ S_x(\nu+\omega_0-2\omega_\mathrm{m}) + S_x(\nu-\omega_0+2\omega_\mathrm{m}) + S_x(\nu-\omega_0-2\omega_\mathrm{m})\right]\\
S_z^{(2)}(\nu) \approx{}& \frac{1}{4}\left[S_z(\nu-\omega_\mathrm{m}) + S_z(\nu+\omega_\mathrm{m})\right] + \frac{1}{16}\left[S_x(\nu+\omega_0+\omega_\mathrm{m}) + S_x(\nu+\omega_0-\omega_\mathrm{m}) + S_x(\nu-\omega_0+\omega_\mathrm{m})\right.\\
&\left.+ S_x(\nu-\omega_0-\omega_\mathrm{m})\right] + \frac{1}{16}\left(\frac{\epsilon_\mathrm{m}}{\Omega}\right)^2 \left[S_x(\nu+\omega_0+2\omega_\mathrm{m}) + S_x(\nu+\omega_0-2\omega_\mathrm{m}) + S_x(\nu-\omega_0+2\omega_\mathrm{m})\right.\\
&\left.+ S_x(\nu-\omega_0-2\omega_\mathrm{m})\right].
\end{aligned}
\tag{D.21}
$$

In the second rotating frame, the static field is along the y axis, the decay rates can be analyzed in a similar way

$$
\begin{aligned}
\Gamma_x &= S_y^{(2)}(0) + S_z^{(2)}(\epsilon_\mathrm{m})\\
\Gamma_y &= S_x^{(2)}(\epsilon_\mathrm{m}) + S_z^{(2)}(\epsilon_\mathrm{m})\\
\Gamma_z &= S_y^{(2)}(0) + S_x^{(2)}(\epsilon_\mathrm{m}).
\end{aligned}
\tag{D.22}
$$

The longitudinal and transverse relaxation time $T_{1\rho\rho}, T_{2\rho\rho}$, under resonance condition $\Omega = \omega_\mathrm{m}$ and assuming $S_x(\omega_0 \pm \Omega \pm \epsilon_\mathrm{m}) \approx S_x(\omega_0)$ with $\Omega, \epsilon_\mathrm{m} \ll \omega_0$, are given by

$$
\frac{1}{T_{1\rho\rho}} = \Gamma_y = \left[\frac{3}{4} + \frac{5}{4}\left(\frac{\epsilon_\mathrm{m}}{\Omega}\right)^2\right] S_x(\omega_0) + \frac{1}{4}S_\Omega(\epsilon_\mathrm{m}) + \frac{1}{4}\left[S_z(\Omega-\epsilon_\mathrm{m}) + S_z(\Omega+\epsilon_\mathrm{m})\right] \tag{D.23}
$$

$$
\frac{1}{T_{2\rho\rho}} = \frac{1}{2}(\Gamma_x + \Gamma_z) = \frac{1}{2T_{1\rho\rho}} + \frac{1}{2}S_z(\Omega) + \left[\frac{1}{4} + \frac{3}{4}\left(\frac{\epsilon_\mathrm{m}}{\Omega}\right)^2\right] S_x(\omega_0) = \frac{1}{T'_{2\rho\rho}} + \frac{1}{2T_{1\rho\rho}} \tag{D.24}
$$

where $\frac{1}{T'_{2\rho\rho}} = \frac{1}{2}S_z(\Omega) + \left(\frac{1}{4} + \frac{3}{4}\left(\frac{\epsilon_\mathrm{m}}{\Omega}\right)^2\right) S_x(\omega_0)$ is defined as the pure dephasing rate in the second rotating frame.

With $\epsilon_\mathrm{m} \ll \Omega$ and $S_\Omega(\Omega \pm \epsilon_\mathrm{m}) \approx S_\Omega(\Omega)$, the longitudinal coherence time in the second rotating frame becomes

$$
\frac{1}{T_{1\rho\rho}} \approx \frac{1}{4}S_\Omega(\epsilon_\mathrm{m}) + \frac{3}{4}S_x(\omega_0) + \frac{1}{2}S_z(\Omega) = \frac{1}{2T_{1\rho}} + \frac{1}{4}S_\Omega(\epsilon_\mathrm{m}) + \frac{1}{2}S_x(\omega_0). \tag{D.25}
$$

The transverse coherence time in the second rotating frame

$$
\frac{1}{T_{2\rho\rho}} \approx \frac{1}{8}S_\Omega(\epsilon_\mathrm{m}) + \frac{3}{4}S_z(\Omega) + \frac{5}{8}S_x(\omega_0). \tag{D.26}
$$

Expressions here can also be obtained by simply setting $\xi_{\epsilon_\mathrm{m}} = 0$ in the amplitude-modulated situation.

ORCID iDs

Guoqing Wang https://orcid.org/0000-0002-1822-8121
Yi-Xiang Liu https://orcid.org/0000-0001-7798-1028
Paola Cappellaro https://orcid.org/0000-0003-3207-594X

References

[1] Hahn E L 1950 Spin echoes *Phys. Rev.* **80** 580–94
[2] Carr H Y and Purcell E M 1954 Effects of diffusion on free precession in nuclear magnetic resonance experiments *Phys. Rev.* **94** 630–8
[3] Meiboom S and Gill D 1958 Modified spin-echo method for measuring nuclear relaxation times *Rev. Sci. Instrum.* **29** 688–91
[4] Ryan C A, Hodges J S and Cory D G 2010 Robust decoupling techniques to extend quantum coherence in diamond *Phys. Rev. Lett.* **105** 200402
[5] Souza A M, Álvarez G A and Suter D 2012 Robust dynamical decoupling *Phil. Trans. R. Soc. A.* **370** 4748–69
[6] Uhrig G S 2007 Keeping a quantum bit alive by optimized π-pulse sequences *Phys. Rev. Lett.* **98** 100504

[7] Yang W and Liu R-B 2008 Universality of Uhrig dynamical decoupling for suppressing qubit pure dephasing and relaxation *Phys. Rev. Lett.* **101** 180403
[8] Biercuk M J, Uys H, VanDevender A P, Shiga N, Itano W M and Bollinger J J 2009 Optimized dynamical decoupling in a model quantum memory *Nature* **458** 996–1000
[9] Mukhtar M, Saw T B, Soh W T and Gong J 2010 Universal dynamical decoupling: two-qubit states and beyond *Phys. Rev.* A **81** 012331
[10] Viola L and Knill E 2003 Robust dynamical decoupling of quantum systems with bounded controls *Phys. Rev. Lett.* **90** 037901
[11] Gordon G, Kurizki G and Lidar D A 2008 Optimal dynamical decoherence control of a qubit *Phys. Rev. Lett.* **101** 010403
[12] Fanchini F F, Hornos J E M and Napolitano R. d. J 2007 Continuously decoupling single-qubit operations from a perturbing thermal bath of scalar bosons *Phys. Rev.* A **75** 022329
[13] Hirose M, Aiello C D and Cappellaro P 2012 Continuous dynamical decoupling magnetometry *Phys. Rev.* A **86** 062320
[14] Laraoui A and Meriles C A 2011 Rotating frame spin dynamics of a nitrogen-vacancy center in a diamond nanocrystal *Phys. Rev.* B **84** 161403
[15] Mkhitaryan V V and Dobrovitski V V 2014 Decay of the rotary echoes for the spin of a nitrogen-vacancy center in diamond *Phys. Rev.* B **89** 224402
[16] Aharon N, Cohen I, Jelezko F and Retzker A 2016 Fully robust qubit in atomic and molecular three-level systems *New J. Phys.* **18** 123012
[17] Stark A, Aharon N, Huck A, El-Ella H A R, Retzker A, Jelezko F and Andersen U L 2018 Clock transition by continuous dynamical decoupling of a three-level system *Sci. Rep.* **8** 14807
[18] Loretz M, Rosskopf T and Degen C L 2013 Radio-frequency magnetometry using a single electron spin *Phys. Rev. Lett.* **110** 017602
[19] Xu X *et al* 2012 Coherence-protected quantum gate by continuous dynamical decoupling in diamond *Phys. Rev. Lett.* **109** 070502
[20] Cai J-M, Naydenov B, Pfeiffer R, McGuinness L P, Jahnke K D, Jelezko F, Plenio M B and Retzker A 2012 Robust dynamical decoupling with concatenated continuous driving *New J. Phys.* **14** 113023
[21] Khaneja N, Dubey A and Atreya H S 2016 Ultra broadband NMR spectroscopy using multiple rotating frame technique *J. Magn. Reson.* **265** 117–28
[22] Saiko A P, Fedaruk R and Markevich S A 2018 Suppression of electron spin decoherence in Rabi oscillations induced by an inhomogeneous microwave field *J. Magn. Reson.* **290** 60–7
[23] Cohen I, Aharon N and Retzker A 2017 Continuous dynamical decoupling utilizing time-dependent detuning: continuous dynamical decoupling utilizing time-dependent detuning *Fortschr. Phys.* **65** 1600071
[24] Farfurnik D, Aharon N, Cohen I, Hovav Y, Retzker A and Bar-Gill N 2017 Experimental realization of time-dependent phase-modulated continuous dynamical decoupling *Phys. Rev.* A **96** 013850
[25] Rohr S, Dupont-Ferrier E, Pigeau B, Verlot P, Jacques V and Arcizet O 2014 Synchronizing the dynamics of a single nitrogen vacancy spin qubit on a parametrically coupled radio-frequency field through microwave dressing *Phys. Rev. Lett.* **112** 010502
[26] Layton K J, Tahayori B, Mareels I M Y, Farrell P M and Johnston L A 2014 Rabi resonance in spin systems: theory and experiment *J. Magn. Reson.* **242** 136–42
[27] Saiko A P, Fedaruk R and Markevich S A 2015 Multi-photon transitions and Rabi resonance in continuous wave EPR *J. Magn. Reson.* **259** 47–55
[28] Teissier J, Barfuss A and Maletinsky P 2017 Hybrid continuous dynamical decoupling: a photon–phonon doubly dressed spin *J. Opt.* **19** 044003
[29] Bertaina S, Vezin H and Chiorescu I 2020 Experimental protection of qubit coherence by using a phase-tunable image drive (arXiv:2001.02417 [cond-mat, physics:quant-ph])
[30] Cao Q-Y *et al* 2020 Protecting quantum spin coherence of nanodiamonds in living cells *Phys. Rev. Appl.* **13** 024021
[31] Wang G, Liu Y-X and Cappellaro P 2020 Observation of high-order Mollow triplet by quantum mode control with concatenated continuous driving (arXiv:2008.06435 [physics, physics:quant-ph])
[32] Doherty M W, Manson N B, Delaney P, Jelezko F, Wrachtrup J and Hollenberg L C L 2013 The nitrogen-vacancy colour centre in diamond *Phys. Rep.* **528** 1–45
[33] Pham L M, Bar-Gill N, Belthangady C, Le Sage D, Cappellaro P, Lukin M D, Yacoby A and Walsworth R L 2012 Enhanced solid-state multispin metrology using dynamical decoupling *Phys. Rev.* B **86** 045214
[34] Bauch E, Hart C A, Schloss J M, Turner M J, Barry J F, Kehayias P, Singh S and Walsworth R L 2018 Ultralong dephasing times in solid-state spin ensembles via quantum control *Phys. Rev.* X **8** 031025
[35] Naydenov B, Dolde F, Hall L T, Shin C, Fedder H, Hollenberg L C L, Jelezko F and Wrachtrup J 2011 Dynamical decoupling of a single-electron spin at room temperature *Phys. Rev.* B **83** 081201
[36] Shim J H, Niemeyer I, Zhang J and Suter D 2012 Robust dynamical decoupling for arbitrary quantum states of a single NV center in diamond *Europhys. Lett.* **99** 40004
[37] Bar-Gill N, Pham L M, Jarmola A, Budker D and Walsworth R L 2013 Solid-state electronic spin coherence time approaching one second *Nat. Commun.* **4** 1743
[38] Jaskula J-C, Saha K, Ajoy A, Twitchen D J, Markham M and Cappellaro P 2019 Cross-sensor feedback stabilization of an emulated quantum spin gyroscope *Phys. Rev. Appl.* **11** 054010
[39] Geva E, Kosloff R and Skinner J L 1995 On the relaxation of a two-level system driven by a strong electromagnetic field *J. Chem. Phys.* **102** 8541–61
[40] Jing J, Huang P and Hu X 2014 Decoherence of an electrically driven spin qubit *Phys. Rev.* A **90** 022118
[41] Yan F, Gustavsson S, Bylander J, Jin X, Yoshihara F, Cory D G, Nakamura Y, Orlando T P and Oliver W D 2013 Rotating-frame relaxation as a noise spectrum analyser of a superconducting qubit undergoing driven evolution *Nat. Commun.* **4** 2337
[42] Joas T, Waeber A M, Braunbeck G and Reinhard F 2017 Quantum sensing of weak radio-frequency signals by pulsed Mollow absorption spectroscopy *Nat. Commun.* **8** 964
[43] Stark A, Aharon N, Unden T, Louzon D, Huck A, Retzker A, Andersen U L and Jelezko F 2017 Narrow-bandwidth sensing of high-frequency fields with continuous dynamical decoupling *Nat. Commun.* **8** 1105
[44] Chen M, Sun W K C, Saha K, Jaskula J-C and Cappellaro P 2018 Protecting solid-state spins from a strongly coupled environment *New J. Phys.* **20** 063011
[45] Bylander J *et al* 2011 Noise spectroscopy through dynamical decoupling with a superconducting flux qubit *Nat. Phys.* **7** 565–70

Supplemental Material

Guoqing Wang (王国庆),[1] Yi-Xiang Liu (刘仪襄),[1] and Paola Cappellaro[1,2,*]

[1] *Research Laboratory of Electronics and Department of Nuclear Science and Engineering, Massachusetts Institute of Technology, Cambridge, MA 02139, USA*

[2] *Department of Physics, Massachusetts Institute of Technology, Cambridge, MA 02139, USA*

I. AVOIDED CROSSING AND POWER SATURATION

We compare amplitude-modulated (this supplement) and phase-modulated (main text) CCD scheme in the ϵ_m dependence experiments. The amplitude-modulated experiments show additional avoided crossing features and non-vanishing components. In Figs. 1(a) and 1(f), the FFT of amplitude modulation has avoided crossing features when the frequency components $\lambda^+ - \lambda^-, 2\omega_m - (\lambda^+ - \lambda^-)$ cross, and this is caused by the power saturation. By adding an additional $\epsilon \cos(2\omega_m t)$ to the H_I in Eq. (1) in the main text and performing the Floquet calculation, we can reproduce such avoided crossing and the non-vanishing $\lambda^+ - \lambda-$ components in Figs. 1(d) and 1(i). As a reference, Figs. 1(e) and 1(j) are simulations with no such additional terms. In addition, to further explore these features, we perform similar experiments but scale down the driving strength $\Omega, \omega_m, \epsilon_m$ by a half in Figs. 1(b) and 1(g) and a quarter in Figs. 1(c) and 1(h). In comparison, the relative splitting of energy levels and the intensity in the region of the avoided crossing around $\epsilon_m \approx \Omega$ are smaller when driving strength is weaker. With smaller power, we are able to measure to higher ϵ_m/Ω. In Figs. 1(b) and 1(g), there is another avoided crossing measured at $\epsilon_m \sim (2\pi)3.5$MHz which is caused by the mixing of the same frequency components as the crossing at $\epsilon_m \sim \Omega$, and this avoided crossing is more prominent than that seen at $\epsilon_m \sim \Omega$, which is another piece of evidence that the avoided crossing is caused by the power saturation. Figure 2(a) shows that the power saturates when the Rabi frequency approaches $(2\pi)7 \sim (2\pi)9$MHz. And in Fig. 2(c) we plot how the peak-to-peak amplitude (blue circles) and the average amplitude (blue triangles) of the waveform depend on the setting value Ω. When ϵ_m approaches $(2\pi)3 \sim (2\pi)4$MHz, the maximum amplitude of the amplitude-modulated driving waveform exceeds the saturation level although the average amplitude is still not saturated. In Fig. 3(b) we simulate the amplitude-modulated waveform with a saturation level of the output voltage setting to 8MHz. In the FFT analysis of the simulated waveform, higher order frequency components such as $2\omega_m, 3\omega_m$ start to appear in Fig. 3(f) for the amplitude-modulated case. Returning to the comparison between amplitude modulation and phase modulation, we show above that the amplitude modulation is limited by the power saturation of the microwave delivery. As for the phase modulation, frequency expansion of the phase-modulated waveform $\Omega \cos(\omega_0 + \frac{2\epsilon_m}{\Omega}\cos(\omega_m t + \phi))$ includes an infinite series of frequency components $\omega_0, \omega_0 \pm \omega_m, \omega_0 \pm 2\omega_m, \cdots$. Larger $\frac{2\epsilon_m}{\Omega}$ results in more prominent side bands. We compare a strong modulation in Figs. 3(c) and 3(g) and weak modulation in Figs. 3(d) and 3(h). The FFT spectra of strong modulation shows more prominent side bands. The region between the dashed lines is the working range of our electronics elements. As a result, the phase modulation is limited by the range of electronic elements.

II. RAW DATA FOR Ω DEPENDENCE EXPERIMENTS

The following figures are raw data and simulations of the experiments in the main text to show the resonance shift by sweeping Ω. Figure 4 and Fig. 5 are the comparisons between data (a) and simulation (b,c,d) of Rabi oscillations under different Ω when $\phi = 0$. Simulations in (b) are calculated by directly evolving the Hamiltonian. (c) and (d) are calculated by summing over the frequency components in the Floquet calculation without and with the RWA correspondingly. The consistency of (b) and (c) serves as a verification that the Floquet approach is a precise way to describe the dynamics of the system. The data shows large differences between (c) and (d) when Ω is small, which indicates that when the ratio of ϵ_m to Ω becomes large, the counter-rotating effects start to appear. To further compare the data with simulation, we add decay factors $\exp(-t/\tau_{i,n})$ with $\tau_{i,n}$ fitted from the Rabi oscillations measured in (a) to the simulations in (c) and (d) and plot the comparisons in Fig. 6 and Fig. 7. The data shows good consistency with the Floquet simulation in (c) where we add the additional modulation term $\epsilon \cos(2\omega_m t)\sigma_y$ to the Hamiltonian in Eq. (1) of the main text. As a comparison, the simulation in (b) is without such additional term. Thus the beating

* pcappell@mit.edu

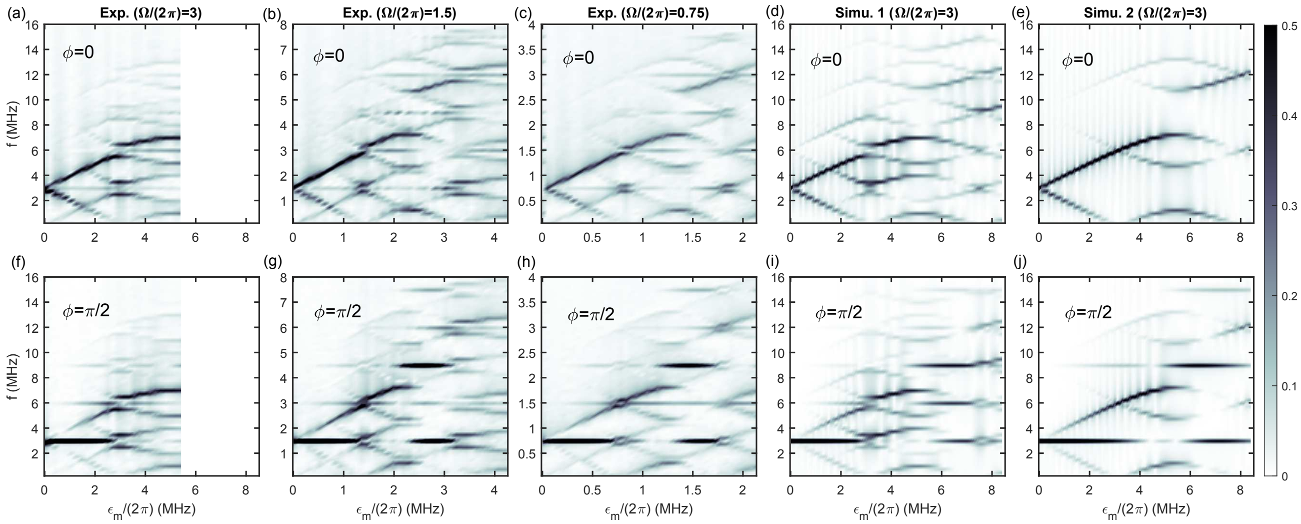

FIG. 1. ϵ_m **dependence of Rabi Fourier spectra**. (a) and (f) are amplitude-modulated experiments measured with $\Omega = \omega_m = (2\pi)3\text{MHz}, \phi = 0, \pi/2$ correspondingly. (b) and (g) are similar experiments measured with $\Omega = \omega_m = (2\pi)1.5\text{MHz}$, which scale as half of the parameters in (a) and (f). (c) and (h) are similar experiments with $\Omega = \omega_m = (2\pi)0.75\text{MHz}$, which scale as 1/4 of the parameters in (a) and (f). (e) and (j) are simulations with Floquet theory using Hamiltonian $H_I = \frac{-\delta}{2}\sigma_z + \frac{\Omega}{2}\sigma_x + \epsilon_m \cos(\omega_m t + \phi)$. (d) and (i) are simulations with Floquet theory using Hamiltonian $H_I^{'} = H_I + \epsilon \cos(2\omega_m t)$ where $\epsilon = 0.4\epsilon_m$ is the strength of the second order modulation.

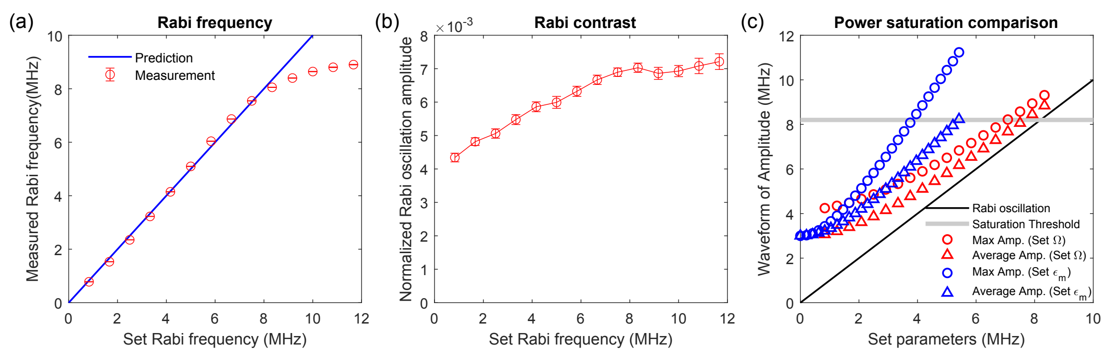

FIG. 2. (a) Rabi frequency versus voltage setting of the arbitrary waveform generator. The x axis is the nominal Rabi frequency as set by the AWG voltage setting and the y axis is the measured Rabi frequency. Red points are the data and blue curve is linear prediction from the voltage setting. (b) Rabi oscillation amplitude under different Rabi frequencies. (c) Power saturation. For red triangles and circles, x axis is the driving strength of the microwave $\Omega/(2\pi)$ in the $\Omega/(2\pi)$ dependence experiments in the main text, y axis for the circles is the maximum amplitude of the waveform and for the triangles is the average amplitude of the waveform. For blue triangles and circles, x axis is the $\epsilon_m/(2\pi)$ in the ϵ_m sweep experiments in Fig. 1(a) and Fig. 1(f) and y axis is shared with the red points. The gray line is the saturation amplitude.

in the oscillations when $\Omega/(2\pi) = 6 \sim 7\text{MHz}$ is the result of avoided crossing caused by the power saturation in the amplitude modulated driving waveform which generates the mixing between $\omega_m + \lambda^+ - \lambda^-, 3\omega_m - (\lambda^+ - \lambda^-)$. Since the power saturation is minuscule in this experiment as shown in Fig. 2(c) in red points, the avoided crossing is almost not visible in FFT spectra in the main text and can be clearly seen as the gradual switch of two frequency components $\omega_m + \lambda^+ - \lambda^-$ and $3\omega_m - (\lambda^+ - \lambda^-)$ as discussed in the main text and Appendix.

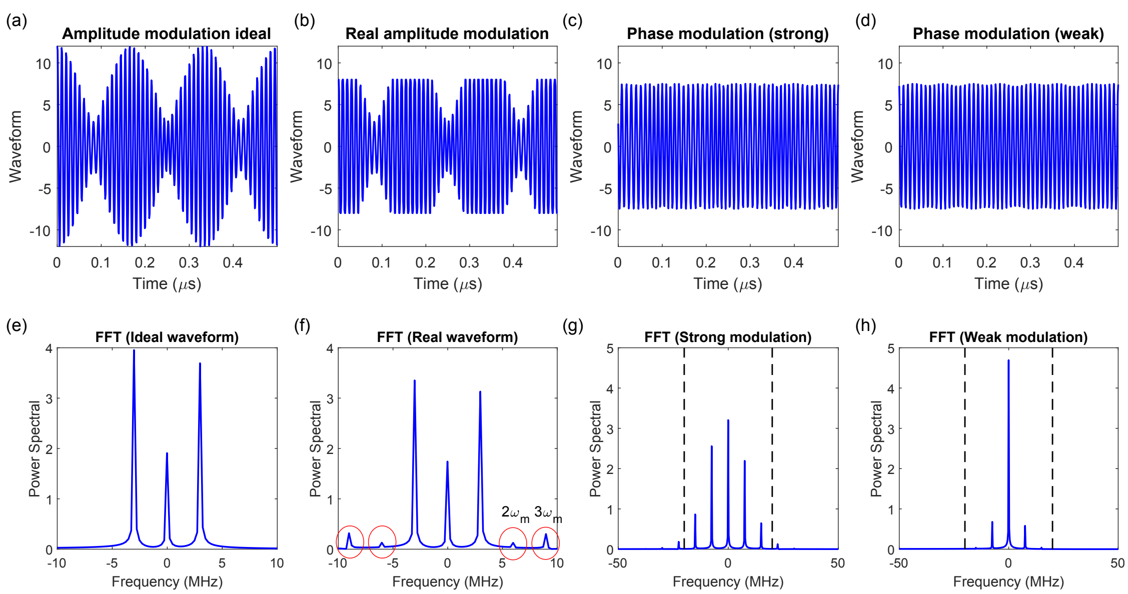

FIG. 3. (a) Ideal waveform for the amplitude-modulated driving, $\Omega\cos(\omega_0 t) - 2\epsilon_m \sin(\omega_0 t)\cos(\omega_m t)$ with $\omega_0 = (2\pi)100\text{MHz}, \Omega = \omega_m = (2\pi)3\text{MHz}, \epsilon = (2\pi)6\text{MHz}$. (b) Effective waveform of the driving term in (a) if we set a saturation level at ± 8. Voltage exceeding this saturation threshold is set to the threshold value. (c) Phase-modulated waveform $\Omega\cos(\omega_0 t + 2\epsilon_m/\Omega\cos(\omega_m t))$ with $\omega_0 = (2\pi)100\text{MHz}, \Omega = \omega_m = (2\pi)7.5\text{MHz}, \epsilon = (2\pi)4.5\text{MHz}$. (d) Phase-modulated waveform $\Omega\cos(\omega_0 t + 2\epsilon_m/\Omega\cos(\omega_m t))$ with $\omega_0 = (2\pi)100\text{MHz}, \Omega = \omega_m = (2\pi)7.5\text{MHz}, \epsilon = (2\pi)1\text{MHz}$. (e-h) FFT spectra of the waveforms in (a-d) respectively. Note that frequency x axis has been shifted by subtracting ω_0 to prominently display the order of the newly appearing peaks.

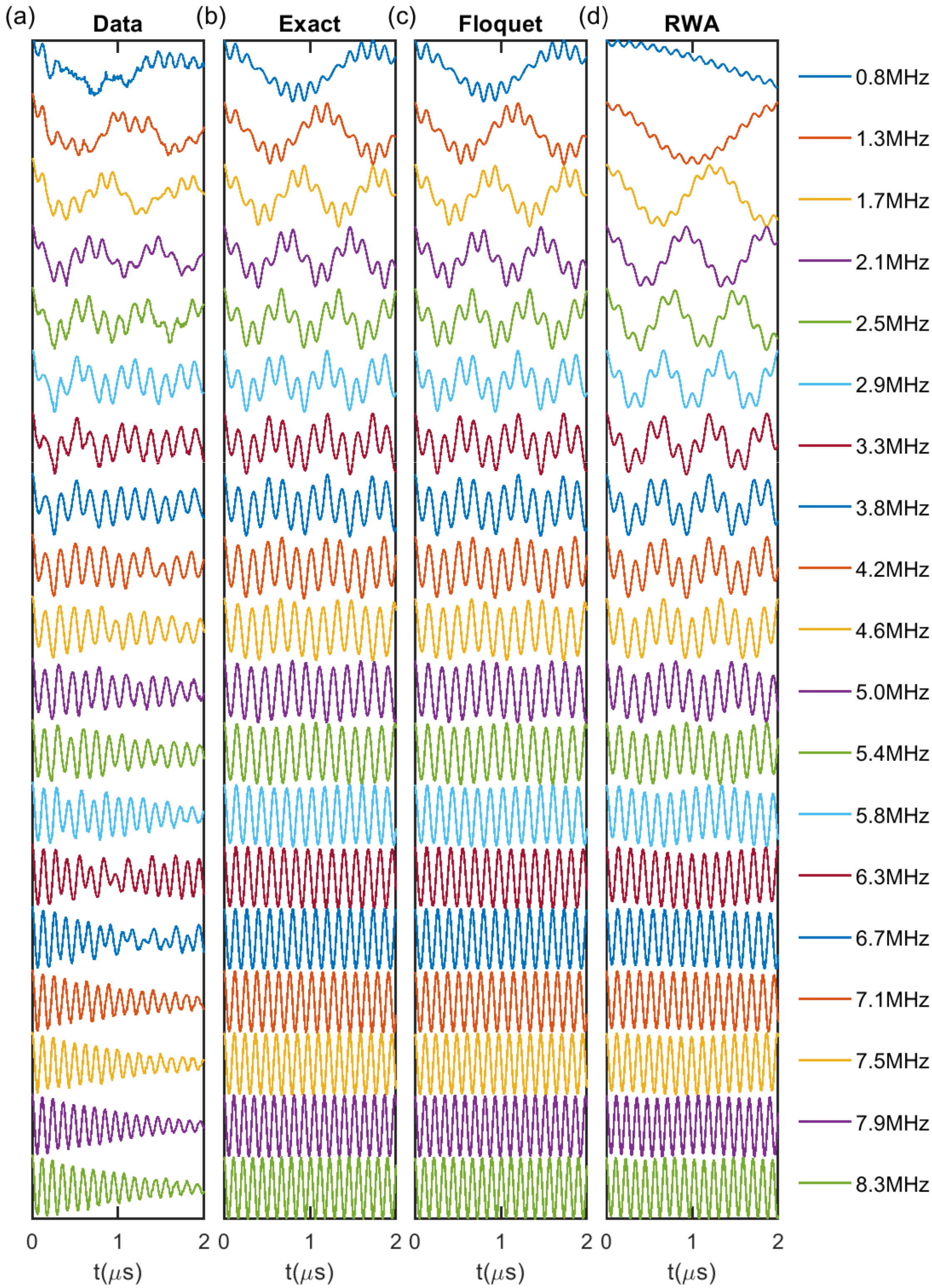

FIG. 4. Raw data and simulations of Rabi oscillations in the Ω dependence experiments in main text with $\phi = 0$. The legend is the value of $\Omega/(2\pi)$. (a) Rabi oscillation data. (b) Rabi oscillation calculated by directly evolving the Hamiltonian in a trotterized manner. (c) Floquet simulation by summing over the first 5 manifolds of triplet frequency components. (d) RWA simulation. Practically the RWA simulation is done in a same way as the Floquet simulation with the counter-rotating terms dropped in the Floquet matrix.

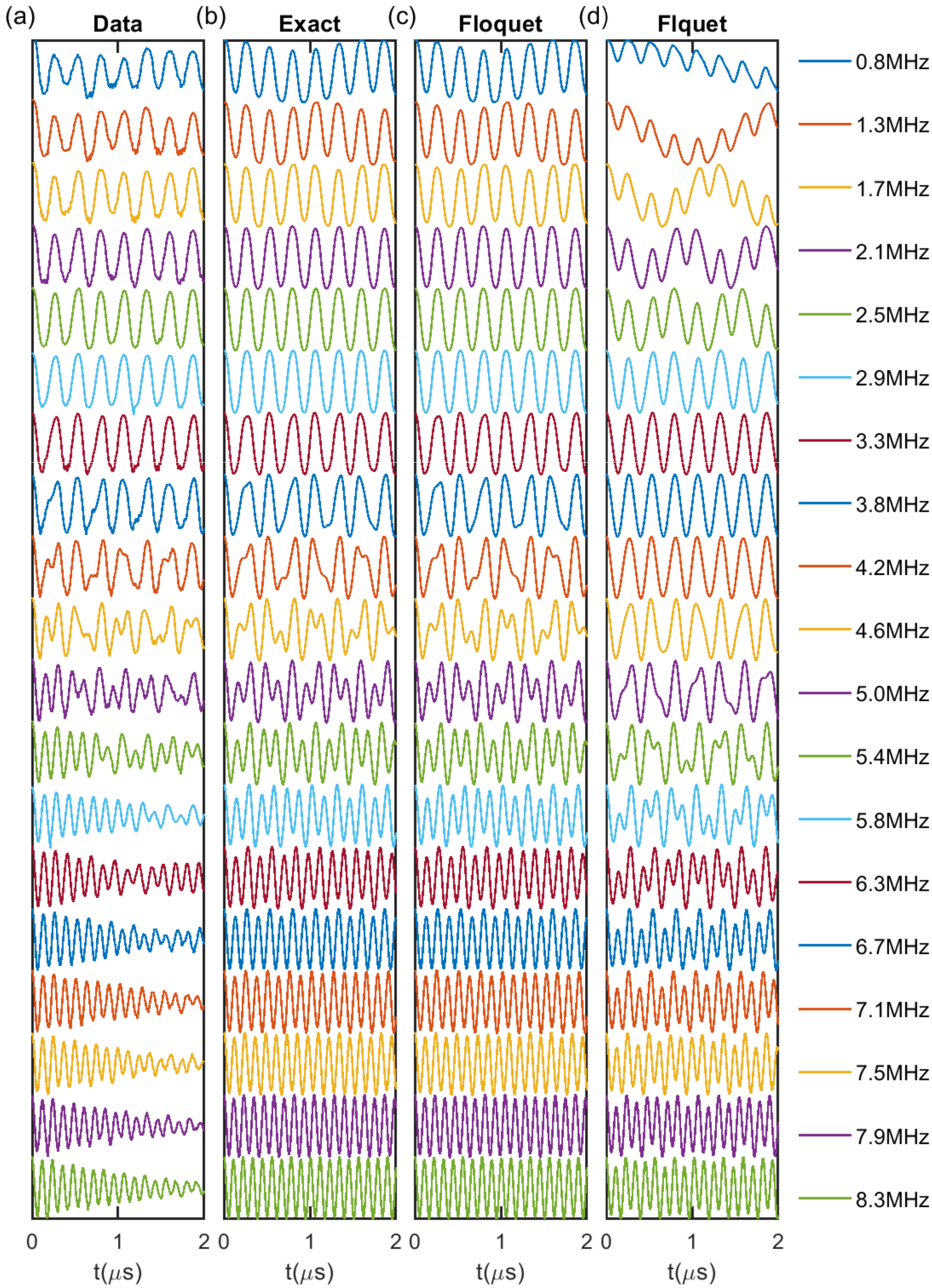

FIG. 5. Raw data and simulations of Rabi oscillations in the Ω dependence experiments in main text with $\phi = \pi/2$. The legend is the value of $\Omega/(2\pi)$. (a) Rabi oscillation data. (b) Rabi oscillation calculated by direct evolving the Hamiltonian in a trotterized manner. (c) Floquet simulation by summing over the first 5 manifolds of triplet frequency components. (d) RWA simulation.

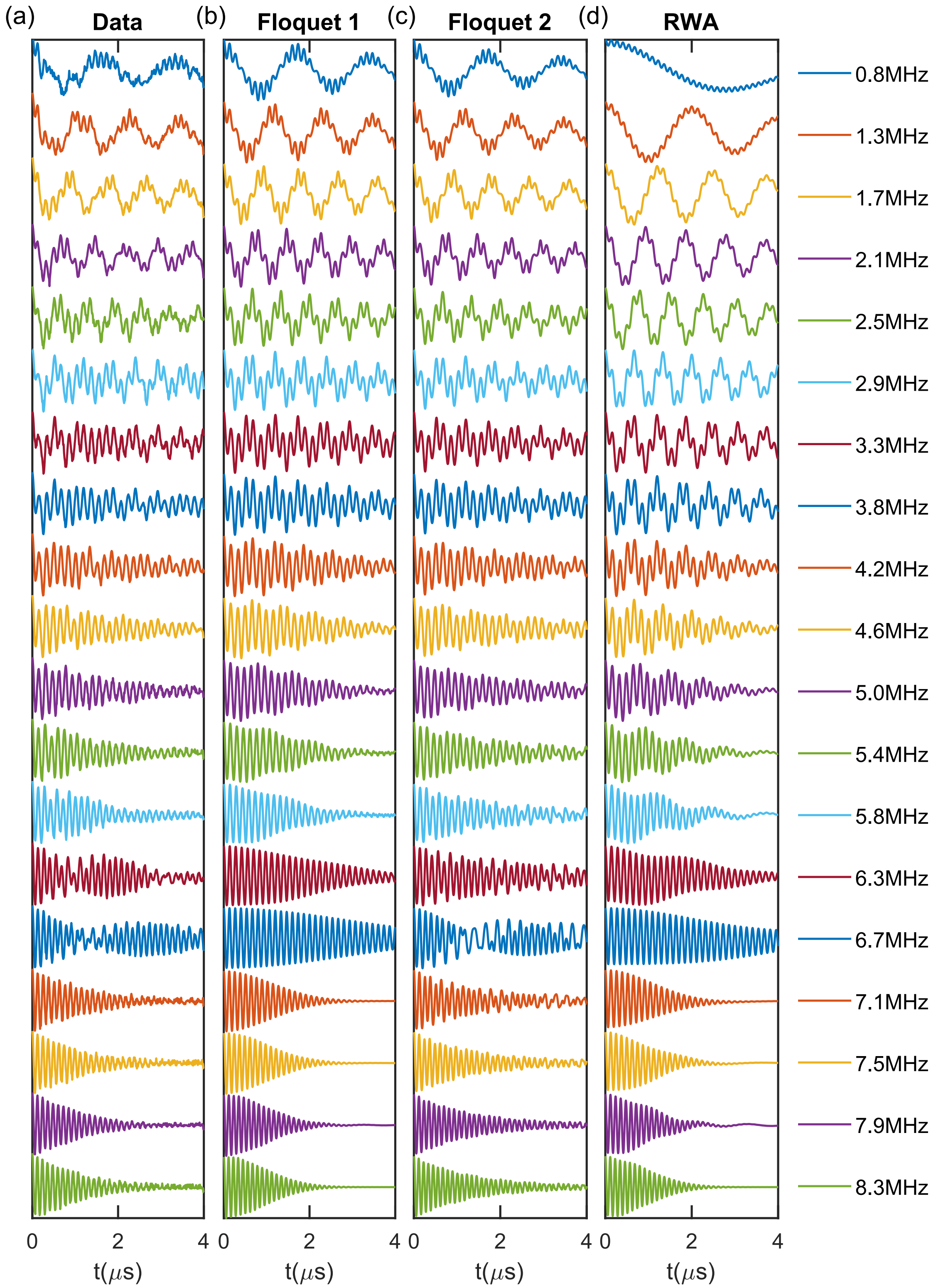

FIG. 6. Raw data and simulations of Rabi oscillations in the Ω dependence experiments in main text with $\phi = 0$. The legend is the value of $\Omega/(2\pi)$. (a) Rabi oscillation data. (b) Floquet simulation with decay. Decay factors $\exp(-t/\tau_{i,n})$ are multiplied to each frequency component with $\tau_{i,n}$ fitted from the experiment data. (c) Floquet simulation with decay and avoided crossing by adding an additional term $\epsilon \cos(2\omega_m t)\sigma_y$ to the Hamiltonian in Eq. (1) of the main text and implementing the Floquet simulation. (d) RWA simulation.

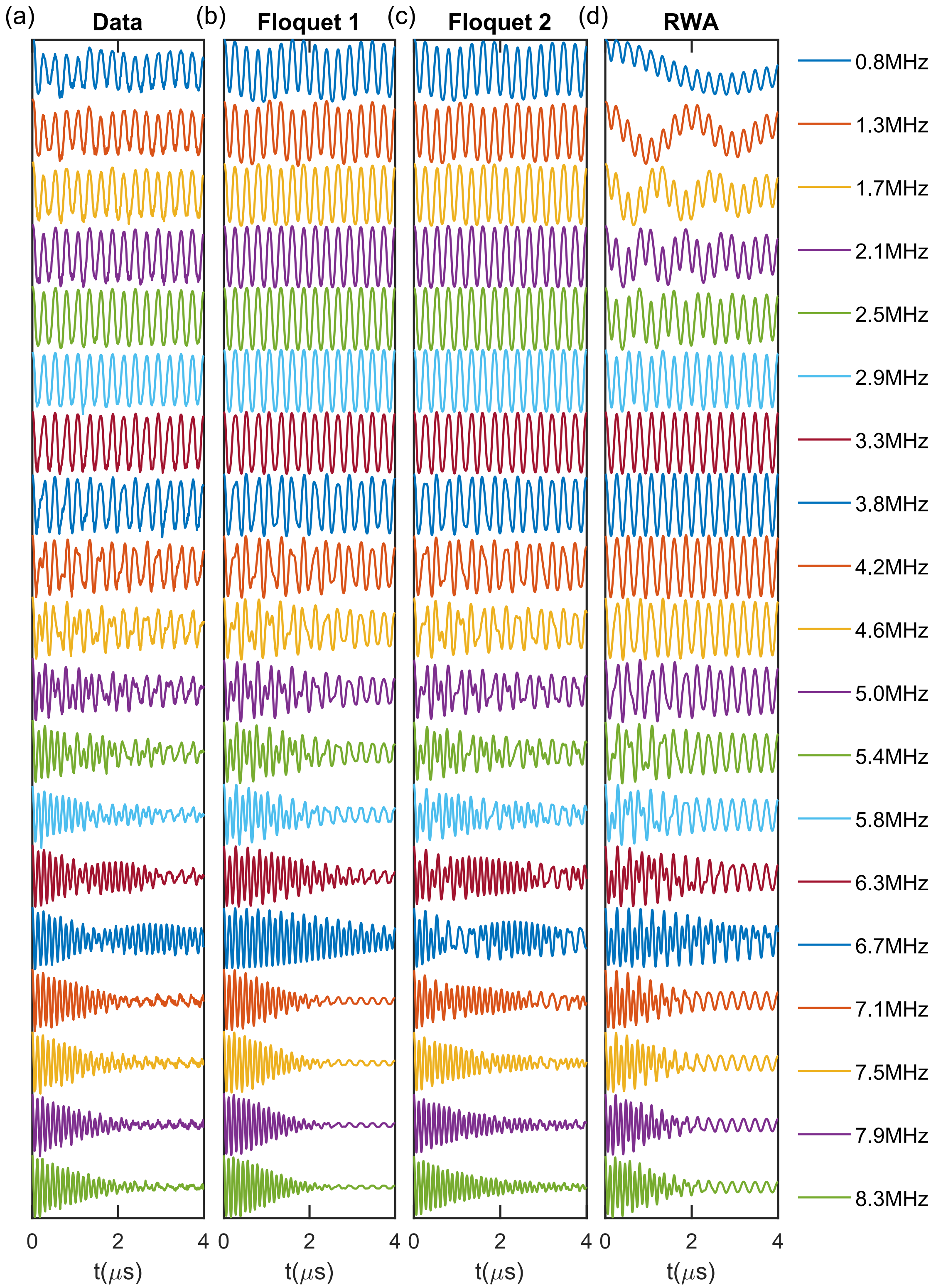

FIG. 7. Raw data and simulations of Rabi oscillations in the Ω dependence experiments in main text with $\phi = \pi/2$. The legend is the value of $\Omega/(2\pi)$. (a) Rabi oscillation data. (b) Floquet simulation with decay. Decay factors $\exp(-t/\tau_{i,n})$ are multiplied to each frequency component with $\tau_{i,n}$ fitted from the experiment data. (c) Floquet simulation with decay and avoided crossing by adding an additional term $\epsilon\cos(2\omega_m t)\sigma_y$ to the Hamiltonian in Eq. (1) of the main text and implementing the Floquet simulation. (d) RWA simulation.